

AD747839

SYNTHESIS OF RARE EARTH COMPOUNDS AND  
STUDY OF THEIR MAGNETIC OPTICAL AND  
SEMICONDUCTING PROPERTIES

IBM Corporation  
Thomas J. Watson Research Center  
Yorktown Heights, New York 10598

ANNUAL TECHNICAL REPORT

June 1972

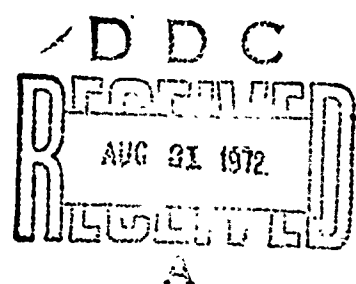
Contract No. DAAH01-71-C-1313

sponsored by

Advanced Research Project Agency  
ARPA Order No. 1588

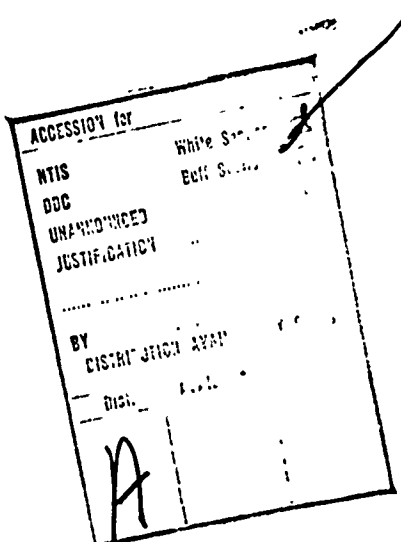
Reproduced by  
NATIONAL TECHNICAL  
INFORMATION SERVICE  
U S Department of Commerce  
Springfield VA 22151

ARPA Support Office - Army Missile Command  
Directorate for Research, Development,  
Engineering and Missile Systems Laboratory  
U. S. Army Missile Command  
Redstone Arsenal, Alabama



NOTICE

"This research was sponsored by the Advanced Research Projects Agency of the Department of Defense under ARPA Order No. 1588 and was monitored by the U. S. Army Missile Command under Contract No. DAAH01-71-C-1313. Views and conclusions expressed herein are the primary responsibility of the author or the contractor and should not be interpreted as representing the official opinion or policy of USAMICOM, ARPA, DOD or any other agency of the Government."



## UNCLASSIFIED

## Security Classification

## DOCUMENT CONTROL DATA - R &amp; D

(Security classification of title, body of abstract and indexing annotation must be entered when the overall report is classified)

1. ORIGINATING ACTIVITY (Corporate author) International Business Machines Corporation Thomas J. Watson Research Center, P. O. Box 218 Yorktown Heights, New York 10598		2a. REPORT SECURITY CLASSIFICATION Unclassified
		2b. GROUP
3. REPORT TITLE  [REDACTED] SYNTHESIS OF RARE EARTH COMPOUNDS AND A STUDY OF THEIR MAGNETIC OPTICAL AND SEMICONDUCTING PROPERTIES		
4. DESCRIPTIVE NOTES (Type of report and inclusive dates) Annual Technical Report (30 June 1971 to 30 June 1972)		
5. AUTHOR(S) (First name, middle initial, last name)  F. Holtzberg, T. R. McGuire, T. Penney, M. W. Shafer and S. von Molnar		
6. REPORT DATE June 72	7a. TOTAL NO. OF PAGES 88	7b. NO. OF REFS 58
8a. CONTRACT OR GRANT NO. DAAH01-71-C-1313	9a. ORIGINATOR'S REPORT NUMBER(S) IBM Project # 2552	
b. PROJECT NO.		
c.	9b. OTHER REPORT NO(S) (Any other numbers that may be assigned this report)	
d.		
10. DISTRIBUTION STATEMENT  Distribution of this document is unlimited.		
11. SUPPLEMENTARY NOTES	12. SPONSORING MILITARY ACTIVITY Advanced Research Project Agency Arlington, Virginia 22209 ARPA Order No. 1588	
13. ABSTRACT: Single crystals of EuO have been grown from melts containing excess Eu-metal. As the concentration of europium metal in the initial melt is increased, the growth temperature is lowered and the crystals become richer in europium. The results of infrared absorption and conductivity measurements are correlated with crystal growth parameters. In order to study the effects of disorder on the physical properties of rare earth magnetic semiconductors, a series of EuS crystals were grown with carrier concentrations varying from $< 10^{18}$ to $10^{20} \text{ cm}^{-3}$ . This study treats the effects of localization on transport due to static potential fluctuations and represents the first successful quantitative description of hopping transport in a band tail. Work has been initiated on the $\text{Gd}_{3-x} \text{V}_x \text{S}_4$ system for similar studies. In contrast to the EuS case the insulating end member has a random distribution of vacancies on cation sites leading to fluctuating repulsive potentials and tailing of the conduction band in which electronic states are localized. The insulating end member is antiferromagnetic and increasing carrier concentration leads to increasing saturation magnetization most probably related to the development of a magnetic spiral. A comparative study of the range of homogeneity in the metallic GdSe system was made. The materials were characterized by resistivity, reflectivity magnetic and x-ray measurements. The system exists over a large range of homogeneity and is characterized by a color change from bright gold to a deep metallic blue. The change in color is directly related to changes in carrier concentration. Magnetic measurements for the mixed valence $\text{Eu}_{1-x} \text{La}_x \text{S}$ and $\text{Yb}_{1-x} \text{Gd}_x \text{S}$ have been made. The results of these measurements have been used to establish the sign and strength of the exchange interactions between the different magnetic species in the more complex $\text{Eu}_{1-x} \text{Gd}_x \text{S}$ system.		

DD FORM 1 NOV 64 1473

UNCLASSIFIED

Security Classification

**UNCLASSIFIED****Security Classification**

14. KEY WORDS	LINK A		LINK B		LINK C	
	ROLE	WT	ROLE	WT	ROLE	WT
Semiconducting ferromagnets						
Europium Chalcogenides						
Synthesis						
Nonstoichiometry						
Disordered systems						
Crystal growth						
Rare earths						
Insulator-metal transition						
$Gd_{3-x}^v S_x^4$						
GdSe						

**UNCLASSIFIED****Security Classification**

**SYNTHESIS OF RARE EARTH COMPOUNDS AND  
STUDY OF THEIR MAGNETIC OPTICAL AND  
SEMICONDUCTING PROPERTIES**

**IBM Corporation  
Thomas J. Watson Research Center  
Yorktown Heights, New York 10598**

**ANNUAL TECHNICAL REPORT**

**June 1972**

**Contract No. DAAH01-71-C-1313**

**sponsored by**

**Advanced Research Project Agency  
ARPA Order No. 1588**

**ARPA Support Office - Army Missile Command  
Directorate for Research, Development,  
Engineering and Missile Systems Laboratory  
U. S. Army Missile Command  
Redstone Arsenal, Alabama**

## FOREWORD

This report describes work performed under Contract DAAH01-71-C-1313 for the ARPA Support Office, Research, Development, Engineering and Missiles Laboratory, U. S. Army Missile Command, Redstone Arsenal, Alabama during the period 30 June 1971 through 30 June 1972. The monitor for this project was R. L. Norman. The principal investigator was F. Holtzberg and the report was written by F. Holtzberg, T. R. McGuire, T. Penney, M. W. Shafer and S. von Molnar. The work was performed at the IBM Thomas J. Watson Research Center. The authors gratefully acknowledge the support of J. B. Torrance who contributed to our understanding of the infrared and magnetic properties of the rare earth chalcogenides, and that of W. A. Thompson and E. S. Kirkpatrick for experimental and theoretical contributions to the EuS studies. The authors are also grateful for the technical assistance of R. A. Figat, H. R. Lilienthal, P. G. Lockwood and J. M. Rigotty, and the support of R. W. Johnson, B. L. Olson, J. D. Kuptsis and W. Reuter who provided the following analytical techniques: solid state mass spectroscopy, classical chemical analysis and quantitative electron probe microanalysis.

## SUMMARY

Single crystals of EuO have been grown from melts containing excess Eu-metal. As the concentration of europium metal in the initial melt is increased, the growth temperature is lowered and the crystals become richer in europium. The results of infrared absorption and conductivity measurements are correlated with crystal growth parameters.

In order to study the effects of disorder on the physical properties of rare earth magnetic semiconductors, a series of EuS crystals were grown with carrier concentrations varying from  $< 10^{18}$  to  $10^{20} \text{ cm}^{-3}$ . This study treats the effects of localization on transport due to static potential fluctuations and represents the first successful quantitative description of hopping transport in a band tail. Work has been initiated on the  $\text{Gd}_{3-x} \text{S}_4$  system for similar studies. In contrast to the EuS case the insulating end member has a random distribution of vacancies on cation sites leading to fluctuating repulsive potentials and tailing of the conduction band in which electronic states are localized. The insulating end member is antiferromagnetic and increasing carrier concentration leads to increasing saturation magnetization most probably related to the development of a magnetic spiral.

A comparative study of the range of homogeneity in the metallic GdSe system was made. The materials were characterized by resistivity, reflectivity magnetic and x-ray measurements. The system exists over a large range of homogeneity and is characterized by a color change from bright gold to a deep metallic blue. The change in color is directly related to changes in carrier concentration.

Magnetic measurements for the mixed valence  $\text{Eu}_{1-x} \text{La}_x \text{S}$  and  $\text{Yb}_{1-x} \text{Gd}_x \text{S}$  have been made. The results of these measurements have been used to establish the sign and strength of the exchange interactions between the different magnetic species in the more complex  $\text{Eu}_{1-x} \text{Gd}_x \text{S}$  system.

## TABLE OF CONTENTS

	<u>Page</u>
1.0 INTRODUCTION	1
2.0 RELATIONSHIP OF CRYSTAL GROWTH PARAMETERS TO THE STOICHIOMETRY OF EuO, AS DETERMINED BY INFRARED AND CONDUCTIVITY MEASUREMENTS	3
2.1 Introduction	3
2.2 Experimental Techniques	4
2.3 Results and Discussion	6
2.3.1 Phase Diagram	6
2.3.2 Crystallization Paths	12
2.3.3 Crystal Growth	15
2.3.4 Crystal Classification	15
2.3.5 Physical Properties	27
2.4 Summary and Conclusion	36
3.0 SYSTEMATICS OF CONDUCTION IN A BAND TAIL: THE EuS SYSTEM	39
4.0 THE MAGNETIC SEMICONDUCTOR $Gd_{3-x}^{3-x} S_x^{4-x}$	50
4.1 Introduction	50
4.2 Experimental	50
4.3 Discussion	56
5.0 THE METALLIC $Gd_x^{x} Se_{1-x}^{1-x}$ SYSTEM	59
5.1 Introduction	59
5.2 Experimental	59
5.3 Results	63
6.0 MAGNETIC STUDIES OF RARE EARTH CHALCOGENIDE MIXED VALENCY SYSTEMS	72
6.1 Introduction	72

	<u>Page</u>
6.2      Experimental	74
6.2.1 $Eu_{1-x}La_xS$ System	74
6.2.2 $Yb_{1-x}Gd_xS$ System	77
6.3      Discussion	77

## LIST OF FIGURES

	<u>Page</u>
Figure 1. Phase diagram for part of the europium-oxygen system.	7
Figure 2. The EuO region of the europium-oxygen phase diagram (see text).	9
Figure 3. Microstructure of three EuO crystals (see text).	18
Figure 4. The infrared absorption of two samples of EuO from Region II showing the absorption lines characteristic of Eu <sup>3+</sup> .	20
Figure 5. The infrared spectrum of several oxygen-rich samples of EuO from Regions I and II at room temperature. The dashed curve is the absorption spectrum for Eu <sub>3</sub> O <sub>4</sub> reduced to 5% of its full intensity for comparison.	22
Figure 6. The infrared spectrum of several Eu-rich samples from Regions IV and V at room temperature.	23
Figure 7. Log <sub>10</sub> conductivity vs temperature for various EuO samples.	30
Figure 8. Log $\rho$ vs 1/T for H = 0 (circles) and H = 32.8 kOe and 20 kOe (triangles), respectively, for samples a and f. The solid line is a fit of $\exp(T_0/T)^{1/4}$ to the data.	38
Figure 9. (a) Log $\rho$ vs 1/T, (b) log R (Hall constant) and $N_H \equiv 1/Re$ vs 1/T.	41
Figure 10. Log $\rho$ vs $T^{-1/4}$ .	43
Figure 11. (a) Band tail density of states (solid) derived from unperturbed states (dashed) using the fluctuation probability distribution (b). (c) Normalized mobility vs energy.	45
Figure 12. Magnetization curves for Gd <sub>3-x</sub> Eu <sub>x</sub> S <sub>4</sub> at 4.2°K. Samples have increasing Gd concentration starting with x = 1/3 for sample 1. The exact values of x have not been determined.	51
Figure 13. Resistivity, $\rho$ , vs reciprocal temperature. The paramagnetic Curie temperatures are $\theta(3) = 16.1^\circ\text{K}$ and $\theta(2) = 22.2^\circ\text{K}$ .	53
Figure 14. Hall coefficient, $e_H/H_a$ and Seebeck coefficient, S, vs reciprocal temperature.	55
Figure 15. Lattice constant $a_0$ as a function of composition x in Gd <sub>x</sub> Eu <sub>1-x</sub> Se.	62

	<u>Page</u>
Figure 16. Resistivity, $\rho$ , as a function of temperature ( $^{\circ}$ K) for four compositions, $x$ , in the $Gd_x Se_{1-x}$ system.	65
Figure 17. Percent reflectance $R$ as a function of $h\nu$ .	67
Figure 18. Carrier concentration, $n$ , derived from experimental composition, $x$ , (see text) as a function of $h\nu$ for which the reflectivity is a minimum. The data is plotted on a log-log scale to demonstrate that $n \propto (h\nu)^2$ in the $Gd_x Se_{1-x}$ system.	68
Figure 19. Paramagnetic Curie temperature, $\theta$ , as a function of composition, $x$ , for $Gd_x Se_{1-x}$ .	70
Figure 20. Lattice constant vs composition for $Eu_{1-x} La_x S$ .	73
Figure 21. Magnetic moment vs applied magnetic field at $4.2^{\circ}$ K for several compositions of $Eu_{1-x} La_x S$ . The dotted curve marks $B_J = 7/2$ is the Brillouin function calculated for d pure paramagnetic behavior at $4.2^{\circ}$ K as a comparison for compositions $x \geq .65$ .	75
Figure 22. Curie temperature and paramagnetic $\theta$ as a function of composition for $Eu_{1-x} La_x S$ .	76
Figure 23. Paramagnetic $\theta$ vs composition for $Eu_{1-x} Gd_x S$ and $Yb_{1-x} Gd_x S$ . The dashed curve is calculated as indicated above.	78

LIST OF TABLES

	<u>Page</u>
Table I      Oxygen content of quenched liquids (solids) in equilibrium with Eu vapor (see text).	13
Table II     Properties of crystals grown in different crystallization regions.	16
Table III    Conductivity and infrared data for EuO crystals.	25
Table IV    Experimental values of transport data and theoretical estimates using $E_o = E_m = 12\text{mV}$ , $E_H = -19\text{mV}$ and $m^* = 1.1m_o$ .	47
Table V $\text{Yb}_{1-x}\text{Gd}_x\text{S}$	77
Table VI    Exchange Interactions ( $^{\circ}\text{K}$ )	79

## 1.0 INTRODUCTION

Through our earlier studies it became evident that disorder plays a significant role in determining the physical properties of the rare earth magnetic semiconducting materials. In such systems transport can be dominated by potential fluctuations of both coulombic and magnetic origin. In contrast to the purely coulombic case, the binding energies of states localized by magnetic fluctuations may be both temperature and magnetic field dependent.

In this report we discuss the properties of three magnetic semiconducting systems. The first section deals with the exploration of the compositional range in EuO. Here detailed descriptions are given for methods of growing single crystals with well defined physical properties and the techniques developed for sample characterization.

The EuS system was selected for studies of the effects of potential fluctuations because it was clear that in this case, with the magnetic fields available to us, it would be possible to separate magnetic and coulombic effects. This section treats the effects of localization on transport due to static potential fluctuations and represents the first successful quantitative description of hopping transport in a band tail.

Another system which naturally lends itself to a band tail description is the  $Gd_{3-x}^v S_{x4} - Th_3 P_4$  type system, where  $v$  denotes a vacancy. Because of a unique structural feature the insulating end member -  $Gd_2 S_3$  is disordered with  $\sim 10^{21}$  vacancies randomly distributed on cation sites. Unlike the EuS system, the band tail in this case is a feature of the insulating end member. Filling vacancies with Gd is therefore expected to perturb the original band structure only at relatively high concentrations.

For comparison metallic GdSe has been investigated. In this case the coulombic effects which give rise to potential fluctuations in EuS and  $Gd_{3-x}^{3-v} S_4$  are suppressed. The system shows a dramatic color change induced in the crystal purely by change in carrier concentration. GdSe is particularly interesting because of its extraordinarily wide range of homogeneity.

In a continuing study of the magnetic properties of mixed valence solid solutions, a comparison is made of magnetic exchange in monosulfides containing divalent and trivalent rare earth elements. The first of these to be studied was the  $Eu_{1-x}^{1-v} Gd_x S$  system which is rather complex since it contains two different magnetic ions. Based on the model described in Section 6 our recent studies of  $Eu_{1-x}^{1-v} La_x S$  and  $Yb_{1-x}^{1-v} Gd_x S$  have established the sign and strength of the exchange interactions between the different magnetic species in  $Eu_{1-x}^{1-v} Gd_x S$ .

## 2.0 RELATIONSHIP OF CRYSTAL GROWTH PARAMETERS TO THE STOICHIOMETRY OF EuO, AS DETERMINED BY INFRARED AND CONDUCTIVITY MEASUREMENTS

### 2.1 Introduction

Europous oxide (EuO) is a ferromagnet<sup>1</sup> which has been studied rather extensively because of its interesting magnetic,<sup>2</sup> magnetooptical,<sup>3</sup> optical,<sup>4,5</sup> and transport properties.<sup>6,7</sup> Samples have been reported to have conductivities which range from insulating to metallic and in some cases to have insulator-metal transitions<sup>6-8</sup> where the conductivity changes with temperature by a factor of 10<sup>13</sup>. The infrared absorption coefficient at a given frequency is also sample dependent and may vary by as much as a factor of 300 at room temperature. Curie temperature variations between doped samples have also been reported.<sup>9-10</sup>

It may be expected that these remarkable variations in the above physical properties of unintentionally doped crystals are related to small deviations from stoichiometry of EuO. From a chemical viewpoint, however, it is difficult to accurately measure such small deviations from stoichiometry. For this reason, we have systematically studied the detailed relationship of the infrared absorption and the conductivity to the stoichiometry of a large number of EuO crystals. Our results show that the variations are indeed due to deviations from stoichiometry. Furthermore, we have used the variations in the infrared and conductivity measurements to characterize the EuO crystals. The method of preparation of crystals of EuO has been described by Guerci and Shafer<sup>11</sup> and by Reed and Fahey.<sup>12</sup> Little information was previously obtained, however, about the details of the liquid-solid-vapor phase relationships and what effect they have on the physical properties of the resulting crystals.

Oliver and Reed<sup>6</sup> have made certain correlations between the electrical conductivity and the crystal growth parameters. They show that insulator-metal transitions occur in samples of EuO grown with excess Eu and attribute this to the presence of oxygen vacancies. In another material, EuTe, Verreault,<sup>13</sup> and Busch, Verreault, and Vogt<sup>14</sup> have used near infrared absorption to characterize

their samples. They have shown that the free carrier absorption may be minimized by varying the annealing time and temperature. Crystals with the lowest absorption were presumed to be closest to stoichiometric EuTe. Evaporated films of EuO have been studied by Ahn and Shafer<sup>10</sup> and by Paparoditis, et al.<sup>15</sup> The former authors correlated changes in the magnetic ordering temperature and other magnetic properties to the film evaporation conditions, while the latter authors investigated the transport properties.

We report here the results of a systematic study of a series of EuO crystals prepared under varying conditions. We have closely examined the relationships of the growth temperature and starting composition to the infrared and conductivity properties of the resulting crystals. On the basis of these properties we were able to classify the EuO crystals into five categories. These results, together with metallographic data, were used to construct a new phase diagram which can be used as a guide for growing EuO crystals having any desired composition within the limits of the diagram. A preliminary description of this work, emphasizing the variations in the infrared and conductivity, has been published elsewhere.<sup>16</sup>

## 2.2 Experimental Techniques

Europous oxide, EuO, is synthesized by reacting Eu-metal and Eu<sub>2</sub>O<sub>3</sub> at high temperatures, i.e., 1300°-2100°C.<sup>17</sup> Because of the volatile nature of Eu-metal (boiling point of 1440°C) and the tendency of EuO to lose Eu at these high temperatures,<sup>18</sup> it is desirable to equilibrate the mixtures and grow the crystals in sealed containers, usually tungsten or molybdenum. The usual procedure was to electron beam weld a cap onto the crucible containing a charge of the desired ratio of Eu-metal to Eu<sub>2</sub>O<sub>3</sub>.<sup>11</sup> Analyses of europium oxide melts cooled from 2150°C in tungsten crucibles showed less than 10 ppma tungsten contamination - an indication of the suitability of this metal as a crucible material. The europium metal and the Eu<sub>2</sub>O<sub>3</sub> were of the highest purity commercially available (99.95 and

5-9's respectively). In the case of the  $\text{Eu}_2\text{O}_3$ , high concentrations of carbon ( $1-5 \times 10^3$  ppm) were consistently found in the as-received state. This impurity was reduced several orders of magnitude by calcining in pure oxygen at  $1350^\circ\text{C}$ , but remained as the major contaminant in the starting as well as the final material. All handling of the materials, i.e., weighing, mixing, etc., was done in a dry box. After reacting the  $\text{Eu}_2\text{O}_3$ -Eu metal mixtures at the desired temperature for sufficient time (several hours to several days) to reach an equilibrium state, they were cooled slowly (6 to 96 hrs) over a preselected temperature interval. In most cases, a Centor tungsten mesh resistance furnace was used as the heating source. The temperature was simultaneously recorded by a Barnes direct reading photoelectric pyrometer and by a W26Re-W thermocouple. The temperature was controlled by a Leeds and Northrup SCR system to  $\pm 0.5^\circ$  in the  $2000^\circ\text{C}$  range.

In addition to these slow-cool crystal growth runs, many samples were rapidly quenched from high temperatures. In most cases, RF heating was used and the crucible containing the charge was quenched to lower temperature in a few seconds by plunging it into a gallium bath.

Selected samples from the crystal growth and quenched runs were analyzed by wet chemical techniques, metallographically, and by infrared and conductivity measurements. Chemically the total europium content was determined by complexometric titration (EDTA). Normal metallographic techniques proved to be very useful in determining the liquidus temperatures and detecting the small quantities of extraneous phases.

The conductivity measurements were made using the four-probe van der Pauw technique except where otherwise stated. Lanthanum-silver contacts were alloyed into the material under an inert atmosphere and provided good ohmic contacts. Current leakage on the surface of the sample and on the holder limited the measurements to about  $10^{13} \Omega$ , corresponding to bulk conductivities of about  $10^{-11} (\Omega\text{-cm})^{-1}$ .

The infrared measurements reported here were performed at room temperature on a Perkin-Elmer Model 301 grating spectrometer. Although measurements were made over the frequency range 500 to 10,000  $\text{cm}^{-1}$  (20 to 1  $\mu$ ), a smaller range of 2000 to 6000  $\text{cm}^{-1}$  (5 to 1.6  $\mu$ ) would be sufficient to characterize EuO samples. The absorption coefficients are calculated from transmission data using the measured thickness and correcting for the 15% reflectivity.

### 2.3 Results and Discussion

#### 2.3.1 Phase Diagram

Guerci and Shafer<sup>11</sup> first showed the feasibility of growing EuO crystals from metal-rich solutions and presented a possible phase diagram for the Eu-EuO system. Reed, Fahey, and Oliver<sup>6,19</sup> have further worked on the problem and noted certain relationships between the physical properties of EuO and the growth conditions. Recent papers by Bedford and Catalano,<sup>20</sup> and Reed and Fahey,<sup>12</sup> have characterized the melting relationships and the crystal growth process and have briefly discussed the variable composition of the EuO phase. The former authors were primarily concerned with the oxygen-rich EuO compositions. In addition, McCarthy and White,<sup>21</sup> from literature data and thermodynamic considerations, proposed a "not impossible" phase diagram for the Eu-Eu<sub>2</sub>O<sub>3</sub> system but did not consider the variable stoichiometry of EuO.

In this work we have shown how the phase boundary between the EuO phase and the liquid plus crystal region varies with temperature, and further we have accurately determined the liquidus curve between EuO and Eu-metal. We have also made detailed correlations between crystals grown from various regions of the diagram and their physical properties.

From the analyses of more than 30 single crystals, grown under different conditions, and many quenched samples it was possible to construct the phase diagram shown in Figs. 1 and 2. This diagram for the europium-rich portion of the

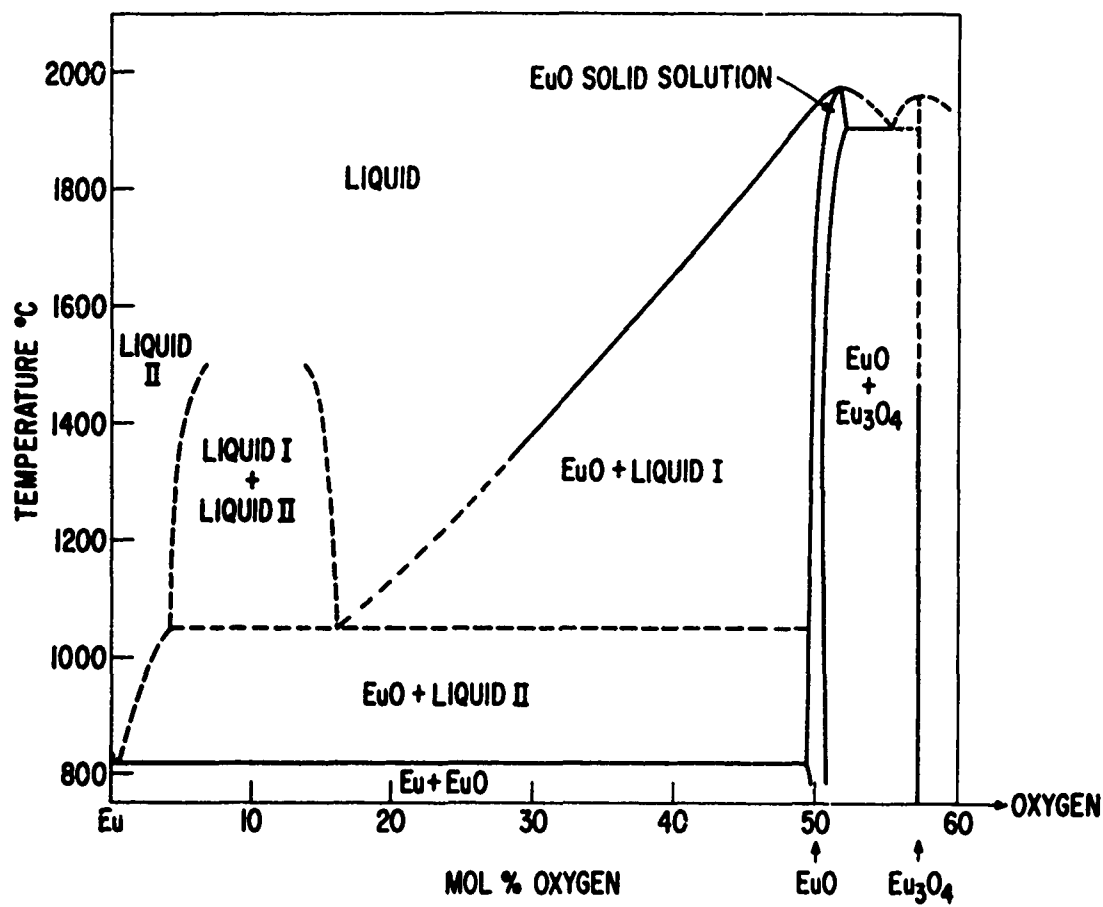


Figure 1. Phase diagram for part of the europium-oxygen system.

europlum-oxygen binary system is constructed as a pseudo-condensed system and shows the relationship between the liquid, solid, and vapor phases which is most consistent with our data. The diagram was determined under the conditions where all reactions were carried out in closed containers. Under these conditions it was not possible to vary the pressure independently - thus for any given Eu/EuO ratio the Eu pressure is determined by the temperature alone.

There are several significant features of this diagram:

1. At high temperatures, stoichiometric EuO does not exist;
2. There is appreciable compositional variation in the EuO phase;
3. EuO crystals can be grown from the liquid phase at lower temperatures than was thought possible;
4. It is possible to control the stoichiometry of EuO crystals by choosing the appropriate growth temperature.

The maximum temperature on the liquidus curve,  $1965 \pm 10^\circ\text{C}$  (Figs. 1 and 2), is the melting point of oxygen-rich EuO. This value is within the error limits of the values reported by Reed and Fahey<sup>12</sup> ( $1980 \pm 20^\circ\text{C}$ ) and by Bedford and Catalano<sup>20</sup> ( $1990 \pm 30^\circ\text{C}$ ). At this temperature, and for all temperatures above about  $1800^\circ\text{C}$ , the EuO phase does not exist with the ideal 1:1 stoichiometry because it preferentially loses europium.<sup>18</sup> The remaining oxygen-rich phase contains trivalent europium and europium vacancies. As the temperature is lowered from about  $1965^\circ\text{C}$ , the EuO phase loses less europium and, starting at about  $1825^\circ\text{C}$ , it is possible to have a liquid in equilibrium with stoichiometric EuO. At still lower temperatures the EuO field crosses over to the Eu-rich side of the 1:1 stoichiometric composition, so that it is possible, at low temperatures, to crystallize europium-rich EuO from the liquid. These crystals probably contain oxygen vacancies, as discussed later in this paper.

We find that the EuO phase field has a significant width over most of the

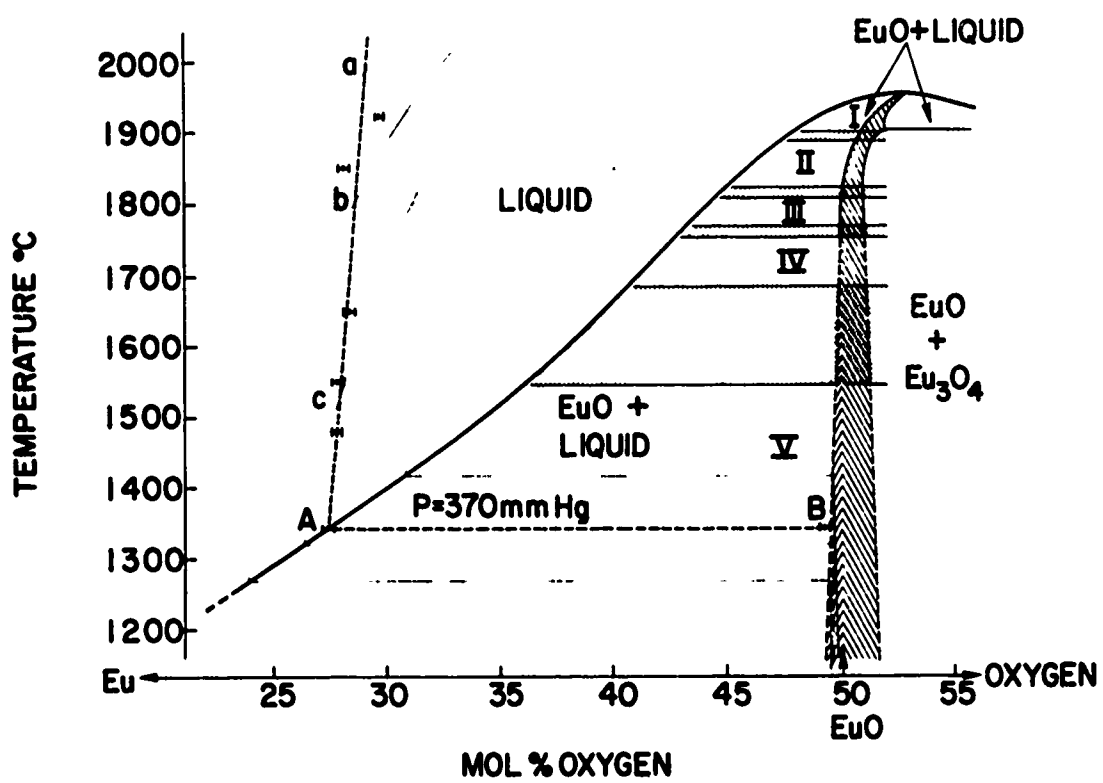


Figure 2. The EuO region of the europium-oxygen phase diagram (see text).

temperature range studied - probably more on the oxygen-rich side than the Eu-rich side. Our estimate of this width is based on data from several sources, since it is difficult using conventional chemical techniques alone to determine compositions within a phase field whose total width is only a few percent. These data are all consistent with a total width in the 2-4% range.

On the oxygen-rich side, the width is estimated from the following evidence: first, Mossbauer measurements by G. Petrich<sup>22</sup> showed the existence of as much as  $\sim 3\%$  Eu<sup>3+</sup> in some single phase crystals. (A 3% concentration of Eu<sup>3+</sup> is indicative of a  $\sim 1.5\%$  concentration of europium vacancies.) Unfortunately, no study was made of the Eu<sup>3+</sup> concentration dependence on the growth temperature of different samples. Secondly, microstructures of several polycrystalline EuO<sub>x</sub> samples, to which various concentrations (1-3%) of Eu<sub>2</sub>O<sub>3</sub> were added, were shown to be single phase after reacting at 1200-1500°C.<sup>23</sup> Finally, chemical analyses of these samples, as well as those of crystals grown with little or no excess Eu-metal, showed a slight difference (1-2%) between the Eu<sup>2+</sup> and the total europium concentrations. The rather consistent results from these three different methods allow us to conclude that the EuO phase field extends to roughly 1-3% on the oxygen-rich side. This conclusion is in agreement with the work of Bedford and Catalano,<sup>20</sup> who report that at 1500°C the solubility limit corresponds to a composition of EuO<sub>1.01</sub>. What we are less certain of is just how the limit varies with temperature.

On the Eu-rich side, the maximum solubility limit is in the  $\sim 1/2$ -1% range, less than on the oxygen-rich side. Our evidence for this estimate is mainly based on low temperature carrier concentration measurements, which showed a maximum of  $6 \times 10^{19}/\text{cm}^3$ . This number ( $\sim 0.2$  mol%) is a lower bound for the width, since some of the electrons are undoubtedly in localized nonconducting states. An upper limit is provided by chemical analyses for total europium, which

yielded a europium excess of  $1\% \pm 1\%$  for those samples showing metallic conductivity.

The exact features of the extreme europium-rich region of the diagram have not been determined with a high degree of accuracy. Therefore, the boundaries (less than 25 mol % oxygen) are shown as dashed lines in Fig. 1. There is some evidence from our quenching experiments that two immiscible liquids exist between about 5 and 20 mol % oxygen. However, because of the extreme surface reactivity of these samples and the small difference in the Eu concentration (99.5 vs 97.8 wt %) we were unable by electron microprobe analyses to verify the expected compositional differences that two liquids should show. The eutectic temperature between EuO and Eu-metal was found to be  $825^\circ \pm 3^\circ\text{C}$  - not measurably different from that of pure Eu-metal ( $826^\circ\text{C}$ ). This indicates that EuO only slightly lowers the freezing point of Eu-metal.

If the europium pressure could somehow be varied independently, a complete P-T-X diagram could be presented. To determine such a diagram, however, a separate europium source, coupled to the reaction vessel and capable of producing and maintaining the desired Eu-pressure, would be required. Under these conditions where pressures other than those attainable in the sealed crucible technique are produced, it is probable that the width of the EuO field on the Eu rich side would be extended by several percent. The point to be emphasized is that the T-X diagram shown in Fig. 1 is just a single surface which cuts across the volume defining the P-T-X diagram for the europium-oxygen system. It cannot even be considered an isobaric section, since the Eu pressure is changing with temperature; therefore, the surface will be curved in the P direction and somewhat irregular in the X. A family of such planes would show the complete P-T-X relationships and make it possible to define the exact crystallization paths.

### 2.3.2 Crystallization Paths

For reasons of clarity, an expanded section of the phase diagram showing the EuO region and the liquidus curve is shown in Fig. 2. The heavy dashed line shows the composition of the liquid and solid phases in equilibrium with pure europium vapor (we will call this the composition line). In order to determine this line, an open crucible containing EuO single crystals, and subsequently the final reaction product, were placed inside a sealed crucible containing a large excess of Eu-metal. In such an arrangement the liquid metal phase, which was present at all temperatures studied, was never in contact with the oxide phase so that the reactions occurred only via the vapor. After holding at the desired temperature for 30-40 hrs the crucible was rapidly quenched and analyzed for total Eu. The results are given in Table I. From the analyses of the Eu-metal residue in the bottom of the sealed crucible, it was evident that little, if any, oxygen is dissolved in the metallic phase. This supports the assumption that for the Eu-rich compositions the total pressure in the closed crucible is essentially that of the vapor pressure of pure europium. The results of the oxide analyses show that the Eu-to-oxygen ratio in the liquid phase remains essentially constant as a function of temperature - a result which is not too surprising since the loss of Eu from the liquid to the vapor phase with increasing temperature is balanced by an increase in the Eu pressure. There is an univariant point at 1355°C (point A) where the composition line intersects the liquidus curve and where three phases, liquid, solid, and vapor, are in equilibrium. Further lowering of the temperature below 1355°C, or the Eu pressure, will result in the liquid being converted to a solid. The composition of this solid, point B in Fig. 2, is oxygen-deficient EuO, and the equilibrium europium pressure is 370 mm Hg - the vapor pressure of Eu at 1355°C. The composition line becomes an isobar only between points A and B - above and below this line, as the temperature is lowered, the composition jumps across the isobars in the direction of lower pressure. For

TABLE I.

Oxygen content of quenched liquids (solids) in equilibrium with Eu vapor (see text).

<u>Quenching Temperature °C</u>	<u>Mol % Oxygen</u>
1920	29.7
1850	28.01
1650	28.57
1560	27.96
1475	27.98
1355	27.04
1345	(49.06)

example, in Fig. 2, where several hypothetical isobars are shown by the light solid lines, the points where they intersect the composition line (a, b, c) show the total compositional changes on cooling and how the composition crosses through a family of isobars. Within the single phase EuO region, the isobars most certainly will run almost vertically and be bunched together on top of each other. Thus, below 1355° the composition line will essentially run parallel to the family of isobars and only small compositional variations will occur as the temperature decreases.

The significance of the 1355°C temperature is that it is the lowest temperature that EuO and liquid oxide can be in equilibrium with europium vapor at its own pressure. Therefore, in the growth of EuO crystals from excess metal solutions, the crystallization path will not be greatly affected by changes in the vapor pressure of europium below about 1355°C. Higher europium pressures would be required to lower this temperature. However, in the normal crystal growth runs, crystalline EuO will be in equilibrium with liquid until the eutectic temperature of about 825°C is reached. The composition of this liquid is essentially that of pure europium metal and is designated as liquid II in Fig. 1.

The exact crystallization paths for compositions close to EuO, where there is no liquid metal present as a distinct phase, have not been determined. However, in these closed crucible experiments, the total composition of the condensed phases is essentially constant during cooling so that the regular vertical crystallization paths applicable to condensed systems can be used.<sup>24</sup>

It is evident from Fig. 2 that the temperature from which the EuO crystallizes, to a large extent, determines its stoichiometry. Since the liquidus curve gives the temperature at which crystallization begins on cooling, it is important that this curve be known rather accurately. For this reason we prepared about ten different compositions, containing between 33 and 50 mol % oxygen, and quenched them from various temperatures after cooling from 2000°C. The temper-

ature where crystallization began was determined by cutting the crucible containing the charge lengthwise, polishing, and then making a microscopic examination. The EuO crystal, which grew at the bottom of the crucible, could easily be distinguished from the fine-grained quenched liquid on top. We have neglected supercooling, since the results were reproducible and yielded a smooth curve. We estimate the error limits on the liquidus curve in Fig. 2 as  $\pm 15^{\circ}\text{C}$ .

### 2.3.3 Crystal Growth

Most crystals were grown by slowly cooling sealed tungsten crucibles, 3" long  $\times$  1/2" diam, containing the desired ratio of Eu metal to  $\text{Eu}_2\text{O}_3$  - as previously discussed. Unfortunately, the resulting crystals are usually highly strained because they are required to freeze in the rigid tungsten container. In order to eliminate this, we used a double crucible technique for a number of the later crystals. In this arrangement an open, thin wall (~ 3 mils) crucible containing the  $\text{Eu}_2\text{O}_3$  pellets, and subsequently the EuO crystal, was placed inside the regular sealed crucible containing the excess Eu-metal. In this technique the EuO crystal is never in contact with the liquid metal - only the vapor. Since the melt freezes in the thin-walled, deformable crucible, the resulting crystals were generally more mechanically sound, and probably more strain-free.

### 2.3.4 Crystal Classification

It is evident from the phase diagram that it is possible to crystallize EuO from a liquid at any temperature within about a  $600^{\circ}\text{C}$  range, i.e.,  $1355^{\circ}$  to  $1965^{\circ}\text{C}$ . Furthermore, the composition of the resulting EuO crystals will vary, depending on the temperature of crystallization. We have confirmed this by growing crystals from various temperatures within this range and, as expected, they have a wide range of stoichiometries and consequently vastly different physical properties. On the basis of the differences in the infrared, conductivity, and metallographic

TABLE II.

Class or Growth Region	Initial Compo- sition Mol % <u>Oxygen</u>	Crystal- lization Temp. °C	Characterization		
			Conductivity	IR	Stoichiometry
I	50-47	> 1890	Insulating 0.45-0.7 eV activation energy	Shows spectrum of $\text{Eu}_3\text{O}_4$	Contains $\text{Eu}_3\text{O}_4$ as second phase
II	47-44	1825-1890	"	$\text{Eu}^{3+}$ ab- sorption lines	Single phase $\text{EuO}$ with Eu vacancies
III	44-42	1780-1825	-	Low ab- sorption <sub>-i</sub> $\alpha < 3 \text{ cm}^{-1}$	Stoichiometric $\text{EuO}$
IV	42-35	1680-1780	Insulator- metal transi- tions 0.3 eV activa- tion energy	Oxygen vacancy absorption	Contains oxygen vacancies
V	< 35	below ~ 1600	Metallic con- ductivity	Free carrier absorption	Many oxygen vacancies

properties, we are able to classify the crystals into five categories and to define the five corresponding temperature regions from which they are grown. These five temperature regions are shown in Fig. 2 by the Roman numerals. Table II summarizes the characteristic properties of typical crystals grown from each of the five regions.

Region I: Crystals grown between the EuO melting point (1965°C) and about 1890°C fall in Region I (Table II). Contrary to what has been reported previously,<sup>12</sup> we were not able to grow single phase crystals from this region. This is because the EuO phase which crystallizes from the liquid in this temperature region is deficient in europium by several percent. Consequently, upon cooling these compositions, the rock salt lattice can no longer remain a stable phase containing such large concentrations of Eu vacancies and they are partially rejected in the form of an Eu<sub>3</sub>O<sub>4</sub> precipitate. We have found as much as ~ 5% Eu<sub>3</sub>O<sub>4</sub> in crystals grown near the melting point. In the phase diagram (Fig. 2), this corresponds to crossing the phase boundary into the two-phase region, EuO plus Eu<sub>3</sub>O<sub>4</sub>.

The fact that europium oxide is Eu deficient at these temperatures is expected if the starting composition is stoichiometric, i.e., 1 Eu to 1 Eu<sub>2</sub>O<sub>3</sub>, and the vapor species is Eu-metal.<sup>18</sup> The liquid will therefore be oxygen-rich. Furthermore, the amount of Eu in the vapor phase will also be somewhat dependent on the free volume in the sealed crucible. In our usual crystal growth runs the crystal, after freezing, filled roughly 30% of the total crucible volume. Even the addition of up to 80% excess Eu-metal will not lower the freezing point or increase the Eu pressure sufficiently to prevent the formation of Eu<sup>3+</sup> in the liquid and its incorporation in the crystal. However, it is unlikely that these volume effects can completely account for the discrepancies between our results and those of Ref. 12.



$1 \text{ Eu}_2\text{O}_3 : 1 \text{ Eu}$   
Slow-Cool



$1 \text{ Eu}_2\text{O}_3 : 1.1 \text{ Eu}$   
Slow-Cool



$1 \text{ Eu}_2\text{O}_3 : 1.1 \text{ Eu}$   
Quench  $1930^\circ\text{C}$

3. Microstructure of three EuO crystals (see text).

Figure 3 shows micrographs for three crystals - one whose initial composition was stoichiometric and the other two contained 10% excess Eu-metal. The  $\text{Eu}_3\text{O}_4$  phase is shown as the needle-like phase in the EuO matrix. The fact that this phase is  $\text{Eu}_3\text{O}_4$  was verified by x-ray, electron microprobe, and infrared analyses. It should be noted that in the quenched crystal the observable needle precipitates are fewer and much smaller in thickness than those in the slow-cooled crystal. This result is expected since it is undoubtedly a diffusion-controlled reaction. Crystals grown in this region are much more readily cleavable than those from other regions - presumably because the second phase precipitates on the cleavable (100) planes. The pure EuO phase, i.e., the remaining 95% of the crystal with no  $\text{Eu}_3\text{O}_4$  precipitate, is still europium deficient, containing europium vacancies.

Region II: Crystals grown and quenched from this region (Table II) are single phase and do not contain any of the  $\text{Eu}_3\text{O}_4$  precipitate which was found in those from Region I. The Region II crystals have the rock salt structure, but are europium deficient - up to  $\sim 2\%$  for those crystals grown near  $1980^\circ\text{C}$ . In these crystals infrared absorption is observed (Fig. 4) which is identified as due to  $\text{Eu}^{3+}$ . The presence of  $\text{Eu}^{3+}$  would be expected in these crystals if there were europium vacancies. In fact, two  $\text{Eu}^{3+}$  ions are necessary for each europium vacancy in order to balance the charge. The observation of  $\text{Eu}^{3+}$ , therefore, implies that the europium deficient crystals of Region II have europium vacancies, although they have not been measured directly. Region II falls in the temperature range of  $\sim 1890$ - $1825^\circ\text{C}$  and includes the liquidus composition containing between  $\sim 47$  and 44 mol % oxygen.

Region III: This region is characterized as the one from which stoichiometric EuO is grown, i.e., where deviations from stoichiometry are minimal. Referring to Fig. 2, it is seen that in Region III the EuO composition, in equilibrium with liquid, falls closest to the ideal 1:1 stoichiometry. Thus, crystals grown and

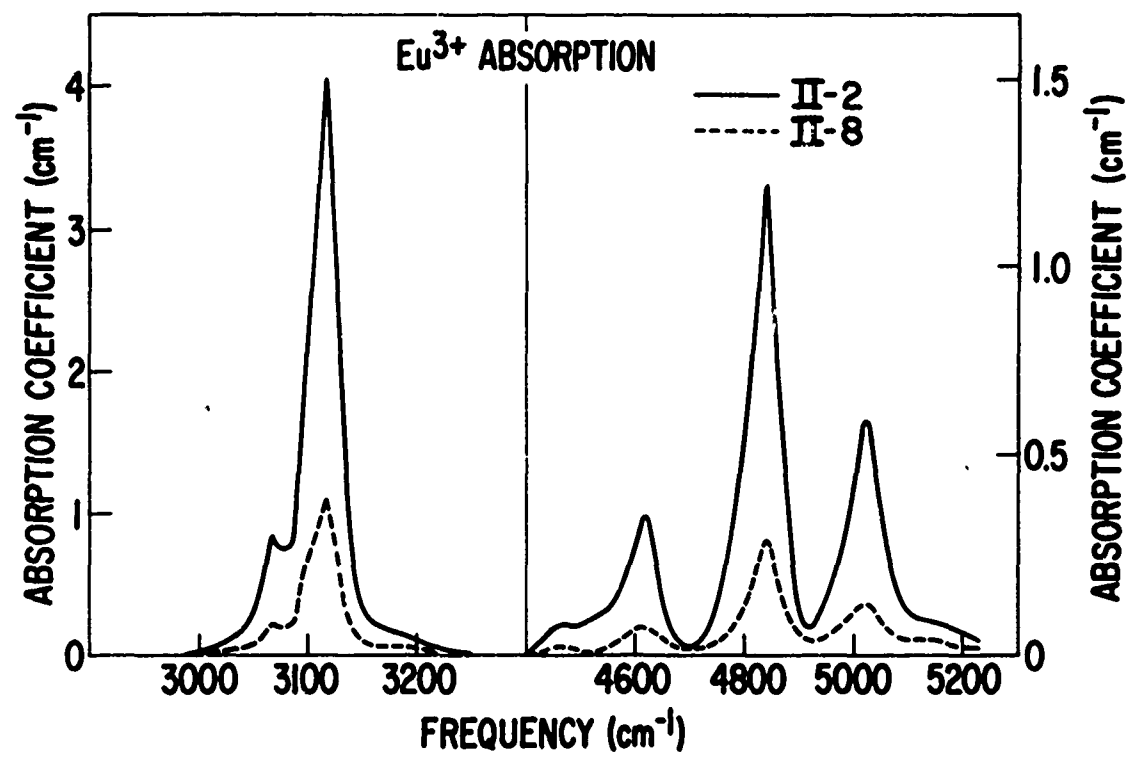


Figure 4. The infrared absorption of two samples of EuO from Region II showing the absorption lines characteristic of Eu<sup>3+</sup>.

quenched from the metal-rich liquid in the temperature range defined by this region ( $\sim 1825^\circ - 1780^\circ \text{C}$ ) will have a minimum of Eu-vacancies ( $< \sim .05\%$ ) and oxygen vacancies ( $< \sim .03\%$ ). It is possible, however, to produce EuO containing trivalent europium in this temperature range. This can be done either by annealing crystals under an europium pressure somewhat lower than it was during growth,<sup>\*</sup> or by reacting an EuO sample with the appropriate quantity of  $\text{Eu}_2\text{O}_3$ .

Concentration gradients are a usual difficulty of melt-grown crystals, particularly those with variable stoichiometry. Such gradients have been observed in most of our EuO crystals. For example, crystals grown from the temperature range defined by Region III (Table II) often contain some trivalent europium in the first-to-freeze portion (bottom) and are slightly oxygen-deficient at the top. For this reason it is very difficult to obtain a reasonably sized crystal which will have the ideal 1:1 (oxygen:europium) stoichiometry throughout the entire crystal. This is the reason why sample III-2 in Table III and Figs. 5 and 6 has traces of Eu vacancies ( $\text{Eu}^{3+}$ ). In another crystal the Eu vacancy concentration was observed to vary from .5 to .05% from one end (first to freeze) to the other. Samples IV-8 and V-1 were both from the same crystal growth run, but showed large differences in their infrared spectra (Fig. 6). In addition, a small radial gradient is sometimes observed. Due to these gradients, it is possible that crystals grown from one particular region near a boundary of an adjacent region will have areas whose properties will not be consistent with those of typical crystals

---

\* The difficulty with controlling the composition by annealing in Eu vapor in the appropriate temperature range is that the location of the Eu isobars as a function of temperature in the single phase EuO region is not known - except for the 370 mm isobar previously discussed. Hence, a trial and error method, where samples are annealed under various Eu pressures, quenched, and then examined until the desired property is obtained, would be necessary.

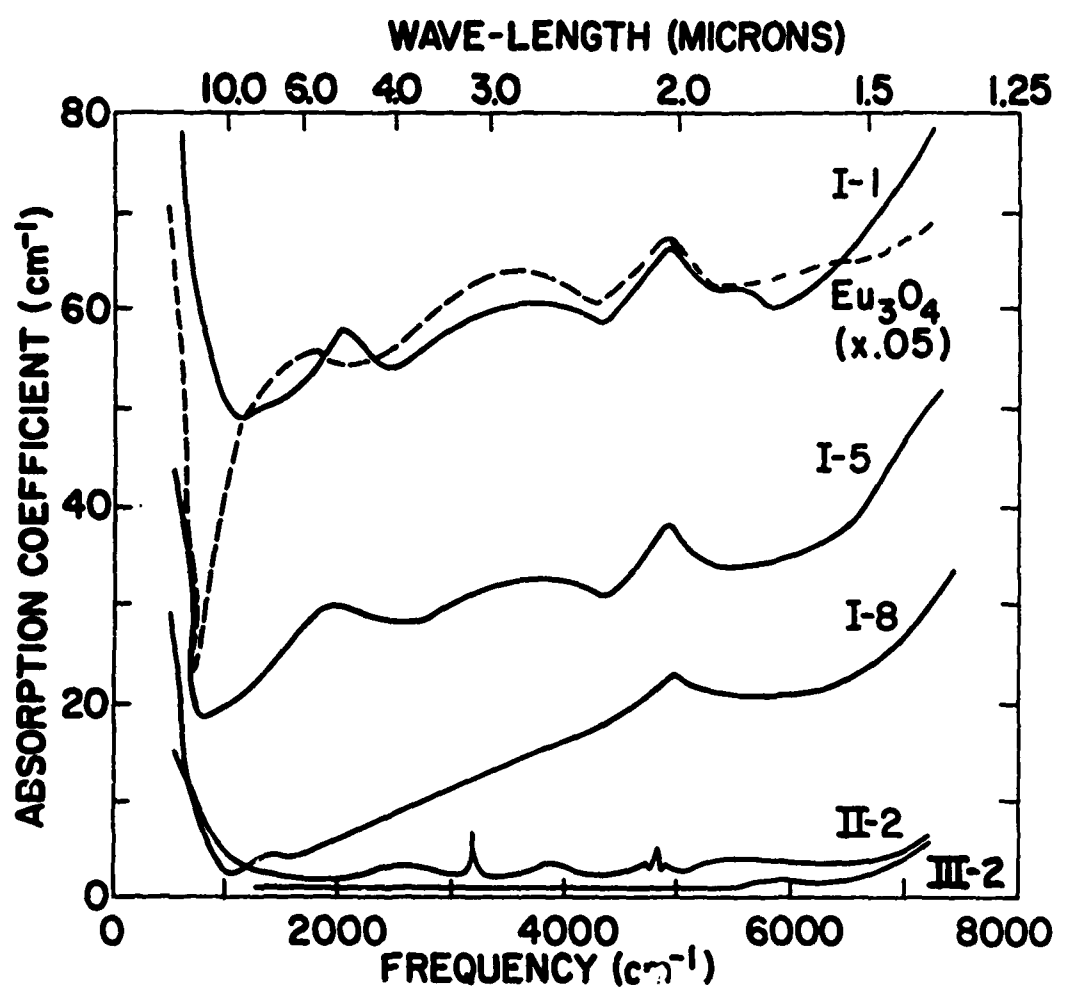


Figure 5. The infrared spectrum of several oxygen-rich samples of EuO from Regions I and II at room temperature. The dashed curve is the absorption spectrum for  $\text{Eu}_3\text{O}_4$  reduced to 5% of its full intensity for comparison.

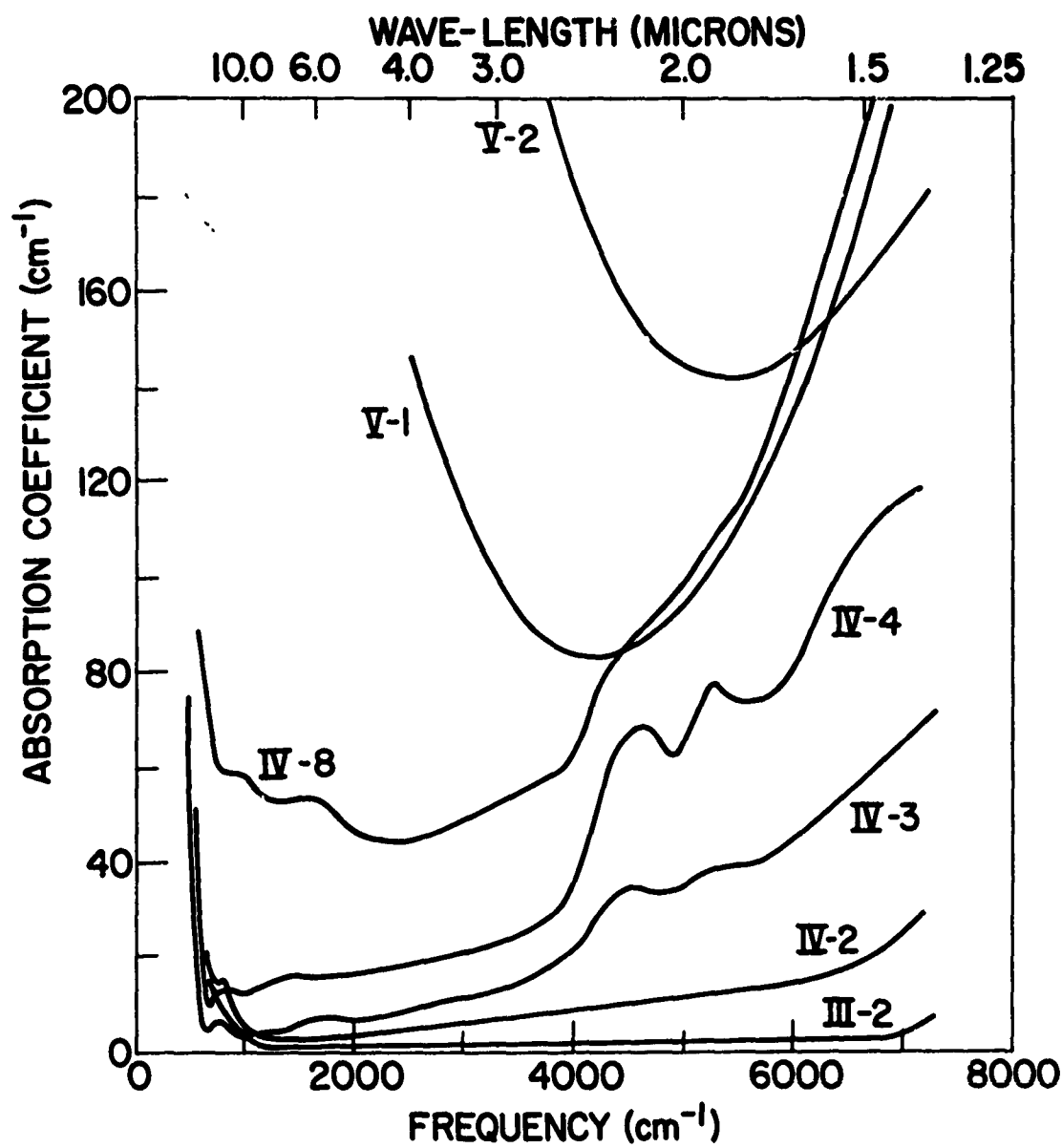


Figure 6. The infrared spectrum of several Eu-rich samples from Regions IV and V at room temperature.

grown from that region. For these reasons, the boundaries between adjacent regions cannot be precisely defined and are, therefore, shown in Fig. 2 by wide "gray areas."

Region IV: As the crystallization temperature drops below about 1780°C the EuO composition becomes europium-rich, as is seen by its phase field extending to the metal-rich side of the stoichiometric composition in Fig. 2. The width of this field increases slightly and rather linearly with decreasing temperature. The maximum width, as previously mentioned, has been estimated from the carrier concentration data to be more than 0.2%. We assume that oxygen vacancies occur in this region. The other alternative, europium interstitials, is highly unlikely because in the closely packed rock salt structure there are no sites for a europium atom of roughly four angstroms in diameter. Also the existence of insulator-metal transitions, which occur in crystals from this region, has been theoretically related to the presence of oxygen vacancies.<sup>25,27</sup> Attempts to prove the existence of vacancies by density measurements yielded results which were inconclusive.

Region V: We define Region V as falling below about 1600°C, even though no abrupt compositional differences between it and Region IV occur - only a continuous increase in the number of oxygen vacancies. The distinction between Regions IV and V is based on the different conductivity behavior exhibited by crystals grown from these two regions, as discussed below.

Careful lattice constant measurements of crystals from all five regions were made and no significant variations were found. Particular effort was made on crystals from Regions II, III, and V by using both Guinier and back reflection diffractometer techniques. The values obtained on crystals from these regions (II, III, and V) were  $5.1446 \pm .0004$ ,  $5.1444 \pm .005$ , and  $5.144 \pm .001$  respectively. From this we can conclude that as we go from oxygen-rich to stoichiometric to

TABLE III.

Run Number	Sample No.*	Starting Comp. (Mol % oxygen)	Growth Temperature (°C)	Conductivity Results (295°K)			Infrared Absorption Results
				$\sigma$ ( $\Omega$ $\text{cm}^{-1}$ )	$\mu$ ( $\text{cm}^2/\text{V-sec}$ )	E (eV)	
13-36A	I-1	49.1	2020				~ 5% $\text{Eu}_3\text{O}_4$
13-114	I-2	50	2000 $\rightarrow$ 1850	$1.8 \times 10^{-8}$	5	.70	~ 4% $\text{Eu}_3\text{O}_4$
47-41	I-3	47.6	1930 $\rightarrow$ 1730				~ 3% $\text{Eu}_3\text{O}_4$
13-41	I-4	47.6	1930 $\rightarrow$ 1790				~ 3% $\text{Eu}_3\text{O}_4$
13-36B	I-5	48.4	1950 $\rightarrow$ 1550	$1.2 \times 10^{-8}$	0.5	.48	~ 2.5% $\text{Eu}_3\text{O}_4$
47-17	I-6	48.4	2000 $\rightarrow$ 1890 Quench	$1.8 \times 10^{-7}$		.46	Large $\text{Eu}_3\text{O}_4$
47-97	I-7	2c <sup>†</sup>	1950 $\rightarrow$ 1700				~ 2% $\text{Eu}_3\text{O}_4$
13-115	I-8	48.0	1950 $\rightarrow$ 1558	$1.3 \times 10^{-8}$	3	.58	~ 1% $\text{Eu}_3\text{O}_4$
47-43	II-1	43.8	1860 $\rightarrow$ 1700	$7.5 \times 10^{-9}$	9	.58	~ 1.5% Eu vac.
13-50	II-2	45.4	1850 $\rightarrow$ 1700	$8 \times 10^{-9}$	1.5	.65	~ 1.0% Eu vac.
13-63	II-3	44.4	1900 $\rightarrow$ 1600				~ 1.0% Eu vac.
47-103A	II-4	2c <sup>†</sup>	1900 $\rightarrow$ 1730				~ 1.0% Eu vac.
47-12A	II-5	2c <sup>†</sup>	1870 $\rightarrow$ 1650 Quench				Low Eu vac.
47-102	II-6	2c <sup>†</sup>	1950 $\rightarrow$ 1800				~ .7% Eu vac.
47-72	II-7	43.6	1825 $\rightarrow$ 1725				~ .6% Eu vac.
47-71	II-8	2c <sup>†</sup>	1940 $\rightarrow$ 1340				~ .2% Eu vac.
13-108	III-1	43.8	1950 $\rightarrow$ 1550	$3 \times 10^{-8}$	5	.58	~ 0% Eu vac. ~ 0% O-vac.
47-71	III-2	2c <sup>†</sup>	1940 $\rightarrow$ 1340				~ 0% Eu vac. ~ 0% O-vac.
47-115	IV-1	42.9	2000 $\rightarrow$ 1400	$4 \times 10^{-6}$	10	.37	
13-108	IV-2	43.8	1950 $\rightarrow$ 1550	$1.4 \times 10^{-4}$		.26	~ .05% O-vac.
71-73	IV-3	-	-	$1 \times 10^{-4}$	14	.3	~ .15% O-vac.
13-89A	IV-4	42.9	1800 $\rightarrow$ 1550	$6.1 \times 10^{-5}$	11	.30	~ .3% O-vac.

TABLE III.‡

Run Number	Sample No.*	Starting Comp. (Mol % oxygen)	Growth Temperature (°C)	Conductivity Results (295°K)			Infrared Absorption Results
				$\sigma$ ( $\Omega$ cm $^{-1}$ )	$\mu$ (cm $^2$ /V-sec)	E (eV)	
13-89B	IV-5	2c†	1800 → 1350	$5.3 \times 10^{-5}$	9	.29	~ .35% O-vac.
47-44	IV-6	43.5	1850 → 1750	$5 \times 10^{-3}$	2	.19	
67-40	IV-7	46.1	1875 → 1350	$7 \times 10^{-3}$	-	.26	~ .35% O-vac.
13-75	IV-8	40.0	1700 → 1400				~ .4% O-vac.
13-75	V-1	40.0	1700 → 1400	13.6	9	Metal	~ .4% O-vac.
13-83	V-2	2c†	1300	27	20	Metal	~ .5% O-vac.

‡ This Table is arranged in order of the systematic changes observed in the infrared spectrum. In this arrangement a general decrease in the oxygen concentration of the starting composition is seen. The deviations are primarily a result of compositional gradients within the crystals and, to a lesser extent, to the variations in quenching rates.

\* The sample number differs from the run number because it was often possible to select several samples from the same crystal growth run. Although the conductivity and infrared data listed in this Table were, in many cases, not made on the same sample, the samples were selected so that these measurements were made on samples from the same area of the crystal.

† In the two crucible crystal growth runs, as described in the text, a large excess of Eu-metal was normally used so that it is meaningless to give the initial starting composition.

euroeuropium-rich, the lattice parameter changes are less than .001 Å. Some line broadening due to strains was observed in most unannealed single crystals, particularly those containing oxygen vacancies (Regions IV and V).

### 2.3.5 Physical Properties

The infrared and conductivity properties of crystals from each of the five regions are briefly summarized in Table II and are discussed in more detail in the following two sections.

**Infrared Measurements:** In order to interpret the infrared results, we consider a series of crystals grown with an increasing percentage of Eu-metal in the starting mixture. In general, we would expect the resulting crystals to also have an increasing percentage of Eu. The infrared absorption spectra observed in such a series of crystals are described in the following paragraphs.

A crystal grown with a stoichiometric starting composition, i.e., 1 Eu-metal to 1  $\text{Eu}_2\text{O}_3$ , exhibits strong infrared absorption over a wide range of frequencies, similar to sample I-1 in Fig. 5. For comparison, the dashed curve is the spectrum for  $\text{Eu}_3\text{O}_4$ ,\* reduced to 5% of its value. The close similarity of these two spectra is interpreted as indicating that  $\sim 5\%$   $\text{Eu}_3\text{O}_4$  is present in sample I-1 as a second phase, in agreement with metallographic results on the same sample. Samples I-5 and I-8 in Fig. 5 were grown with increasing Eu-metal in the starting material and show a decreasing intensity of  $\text{Eu}_3\text{O}_4$ -like absorption. This decreasing amount of second phase is expected as the Eu content of the crystals increases through the series. Crystals which show this absorption spectrum are assigned to Region I. The minimum amount of  $\text{Eu}_3\text{O}_4$  detectable is approximately 0.2%. As we have seen, this infrared technique is able to give information about both the concentration and composition of the second phase.

---

\* The  $\text{Eu}_3\text{O}_4$  was prepared by reacting  $\text{EuO}$  and  $\text{Eu}_2\text{O}_3$  in a sealed crucible at 1700°C.

For crystals grown with more than 53 mol% Eu in the starting material, the  $\text{Eu}_3\text{O}_4$ -like absorption has disappeared, but there remain sharp sets of absorption lines near  $3120$  and  $4850 \text{ cm}^{-1}$ , as shown in Fig. 4 and sample II-2 in Fig. 5. These lines correspond to transitions within the  $4f(^6, ^7F_J)$  multiplet<sup>26</sup> of  $\text{Eu}^{3+}$ , so that the frequencies of these lines are characteristic of  $\text{Eu}^{3+}$ . The presence of  $\text{Eu}^{3+}$  indicates the presence of Eu vacancies as described earlier. The intensities of the  $\text{Eu}^{3+}$  lines are therefore proportional to the number of Eu vacancies in the  $\text{EuO}$  rock salt lattice. If we compare the strongest intensity observed in the samples for the main  $3120 \text{ cm}^{-1}$  line to the estimated  $\sim 4\%$   $\text{Eu}^{3+}$  (or  $\sim 2\%$  Eu vacancies) for the maximum width of the  $\text{EuO}$  field on the Eu deficient side, we get a calibration factor of  $.25 \pm .1\%$  Eu vacancies per  $\text{cm}^{-1}$  absorption strength. Although the absolute value of this factor is somewhat uncertain, the relative concentrations obtained using it are reliable. Using this technique we estimate that we can detect as little as  $\sim .05\%$  Eu vacancies, significantly lower than that which is routinely detectable using the Mössbauer effect.

As we continue through the series of crystals grown with increasing Eu-metal, the Eu vacancy ( $\text{Eu}^{3+}$ ) absorption gradually disappears (e.g., II-2 and II-8 in Fig. 4) and new absorption appears and increases in intensity (e.g., IV-2, IV-3, and IV-4 in Fig. 6). In this series there are some samples, between those showing Eu vacancy absorption and those showing the new absorption, where the absorption intensity has fallen to a minimum (e.g., III-2 in Figs. 5 and 6). These crystals are identified as those closest to 1:1 stoichiometry and are classified into Region III. They are quite transparent in the infrared above  $600 \text{ cm}^{-1}$  ( $16 \mu$ ) and below  $7500 \text{ cm}^{-1}$  ( $1.3 \mu$ ), i.e., above the lattice vibrational absorption and below the electronic absorption edge. In this frequency range, the absorption coefficient is typically  $0.3\text{--}5.0 \text{ cm}^{-1}$ ; those crystals with lower absorption probably have fewer physical defects and chemical impurities. It should be

noted that in order to obtain stoichiometric crystals of EuO using the growth technique described earlier, the starting composition must have  $\sim$  57% europium.

We expect that crystals grown from starting compositions with more Eu than that necessary to grow stoichiometric EuO will contain excess Eu. The infrared spectra of these crystals shows an increasing intensity of absorption similar to that observed in samples IV-2, IV-3, and IV-4 in Fig. 6. We naturally associate this increasing absorption to the increasing excess of Eu in the crystal or, equivalently, to the increasing number of oxygen vacancies. The disorder caused by these vacancies gives rise to "band tailing,"<sup>27</sup> i.e., broad absorption below the absorption edge which increases with increasing frequency, as shown in the samples in Fig. 6. The two broad absorption lines centered at  $\sim$  4700 and  $\sim$  5300  $\text{cm}^{-1}$  (most clearly seen in sample IV-4 in Fig. 6) are believed to be excitations of electrons trapped in the vacancies.<sup>27</sup> Crystals which have this absorption spectrum are classified into Region IV. The intensity of this absorption spectrum is expected to be proportional to the number of oxygen vacancies and can, therefore, be used to approximate their concentration. As a measure of this concentration we use the following calibration factor:  $.004 \pm .002\%$  oxygen vacancies per  $\text{cm}^{-1}$  absorption at  $5000 \text{ cm}^{-1}$ , determined in a way similar to the  $\text{Eu}^{3+}$  factor described earlier. (This factor is, of course, somewhat arbitrary and should be useful mainly for determining the relative concentration of oxygen vacancies.)

Crystals grown with more Eu-metal are expected to have more oxygen vacancies and do show stronger absorption in the infrared. Above a certain concentration, a new type of absorption is observed which rises at lower frequencies, as seen in samples V-1 and V-2 in Fig. 6. These samples are classified into Region V and the absorption is free carrier absorption, due to the relatively high room temperature conductivity of these samples. (The free carrier absorption which rises at lower frequencies should not be confused with the sharply rising lattice absorption near  $600 \text{ cm}^{-1}$ , present in all samples of EuO.)

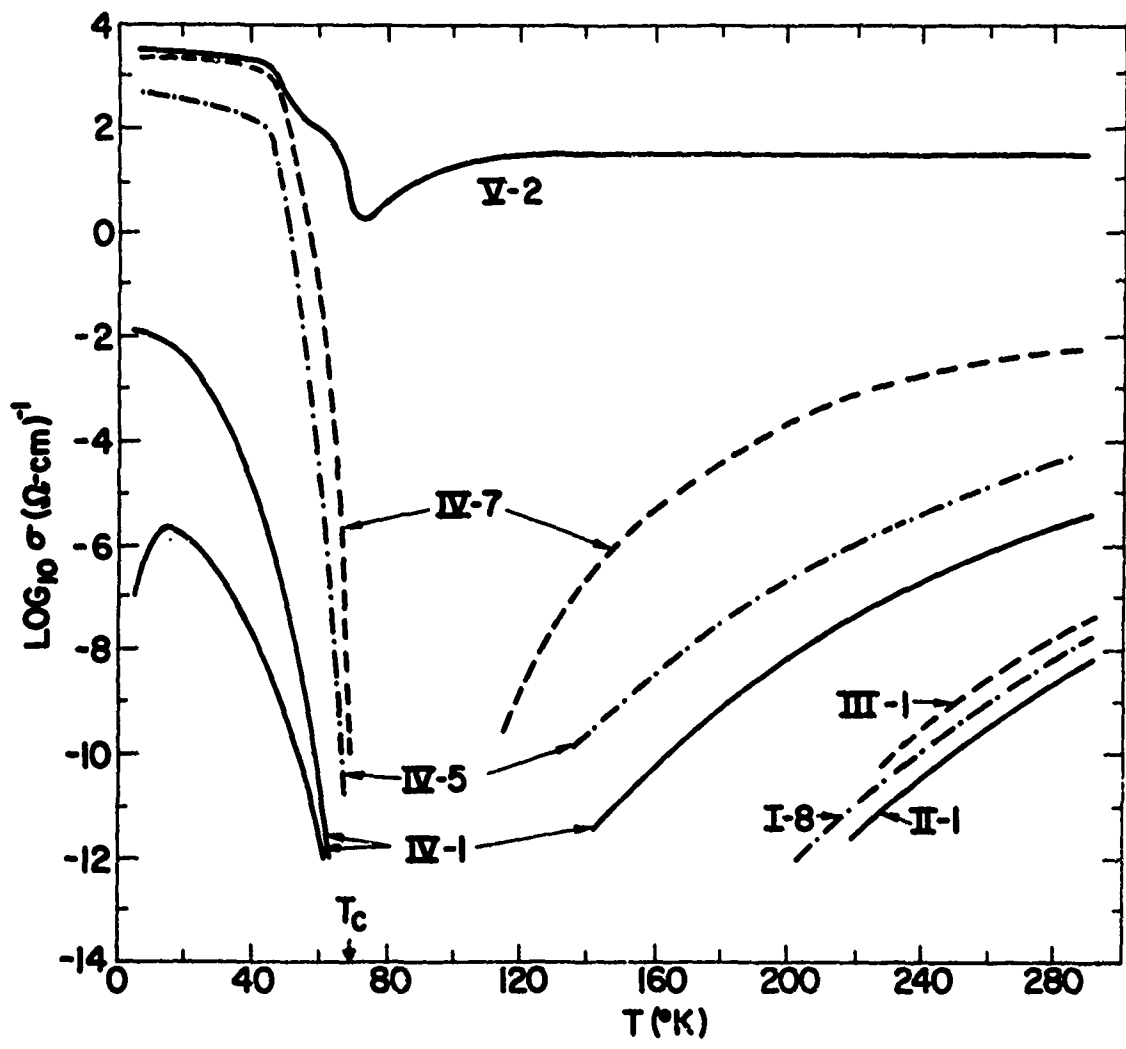


Figure 7.  $\log_{10}$  conductivity vs temperature for various EuO samples.

**Electrical Conductivity Measurements:** The electrical conductivity of samples from Regions I, II, and III show similar insulating behavior. All crystals from these regions have room temperature conductivities of  $10^{-8}$ - $10^{-6}$  ( $\Omega\text{-cm}$ ) $^{-1}$  and room temperature activation energies in the range 0.45-0.7 eV (Table II). Hall effect measurements at room temperature show that conduction is n-type with mobilities,  $\mu$ , in the range 0.5 to 5  $\text{cm}^2/\text{V}\text{-sec}$  and carrier concentrations,  $n$ , of  $10^{10}$  to  $10^{11}/\text{cm}^3$  assuming a single band. In fact, the random potentials due to  $\text{Eu}^{3+}$ , Eu vacancies, and impurities probably smear out the bottom of the conduction band. The lowest energy states in this band are more localized and have lower mobilities than the higher energy states. The conduction in such a band, due to thermal activation, will be given by an integral of the product of the mobility, density of states, and Fermi distribution function. The measured values of  $\mu$  and  $n$  are therefore average values, will depend on the shape of the band tail, and will vary from sample to sample as observed. Hall effect measurements vs temperature on sample II-1 show that the exponential decrease in conductivity below room temperature is due to changes in carrier concentration and not mobility.

The crystal with conductivity labeled III-1 in Fig. 7 exhibited a very weak and flat infrared absorption similar to III-2 in Fig. 5. With increased sample thickness a very small  $\text{Eu}^{3+}$  absorption is observed. The conductivity curve III-1 therefore does not represent exact stoichiometry but a very close approach from the oxygen-rich side.

In Region IV the crystals have excess Eu and hence oxygen vacancies, which give rise to dramatic effects in the conductivity. Below 40°K conduction is metallic while at high temperature it exhibits a thermally activated energy of 0.3 eV compared with ~ 0.6 eV for Regions I, II, and III. Room temperature conductivities are typically  $10^{-4}$  to  $10^{-2}$  ( $\Omega\text{-cm}$ ) $^{-1}$ . Mobilities are of order 10 at room temperature and 100 at 5°K. The most dramatic effect of oxygen vacancies on samples of EuO is in that between 69° and 40°K the conductivity may increase

by more than 13 orders of magnitude as the sample orders ferromagnetically (Fig. 7). This insulator-metal transition is characteristic of samples from Region IV and has been described in detail elsewhere.<sup>6-8</sup>

Kasuya<sup>25</sup> has proposed a model for this insulator-metal transition based on the existence of oxygen vacancies. According to this model neutral oxygen vacancies, since they differ from  $O^=$  by two charges, are analogous to He atoms rather than the more common hydrogenic model used for singly charged impurities. The result is that the ground state of the impurity is the singlet,  $^1S(1s\uparrow 1s\downarrow)$ , formed from two electrons with oppositely paired spins. In this model some of the triplets,  $^3S(1s\uparrow 2s\uparrow)$ , with parallel spins and one electron in a larger 2s orbit, may be hybridized with the bottom of the band forming delocalized, conducting states. Above the ferromagnetic ordering temperature ( $T_c = 69.3^\circ K$ ) conduction occurs by thermal activation (0.3 eV) from the  $^1S$  ground state to those hybridized band states. Below  $T_c$ , the increasing magnetization lowers the parallel spin  $^3S$  with respect to the  $^1S$  reducing the activation energy and increasing conduction. Finally, when the  $^1S$  and  $^3S$  are at the same energy the activation energy vanishes and metallic conduction occurs. In an isolated Helium atom, the state  $^3S(1s\uparrow 2s\uparrow)$  is bound. However, since the distances between oxygen vacancies are random, there will be distribution in the  $^3S$  energies. For a sufficiently high density of vacancies the highest  $^3S$  states will hybridize with the band while the lowest will not. The number of carriers observed at low temperature is therefore some undetermined fraction of the total number of oxygen vacancies and hence a lower limit on the oxygen vacancy concentration.

An alternative model, the bound magnetic polaron (or magnetic impurity state model), also accounts for the insulator-metal transition on the basis of oxygen vacancies.<sup>27</sup> According to this model, the carrier concentration at low temperatures is approximately equal to the number of oxygen vacancies, and not just a lower bound.

Von Molnar<sup>28</sup> and Oliver, et al.,<sup>6</sup> have observed that some samples showing the insulator-metal transition have conductivities which decrease with decreasing temperature below 10-15°K. We had great difficulty in reproducing this behavior, which appears intermediate between Regions III and IV. Nearly all of our crystals have either unmeasurably low, or metallic conductivities below 50°K. In one case (IV-1) we found a crystal which appeared homogeneous at high temperatures but very inhomogeneous at low temperatures. For example, using only two of the four contacts at 7°K, the conductance between one set of adjacent contacts was about four decades larger than between the other three sets of adjacent contacts, while at room temperature they were all nearly the same. The result was that only two probe measurements could be made at low temperature, while at high temperature four-probe van der Pauw measurements were also possible. Figure 7 shows two sets of two-probe data for this sample. The two-probe conductance values ( $\Omega^{-1}$ ) have been translated to conductivity ( $\Omega^{-1}\text{-cm}^{-1}$ ) by comparison of the two- and four-probe values at high temperature.<sup>29</sup>

In Region V the conductivity is metallic at high temperature as well as low temperature. According to the He model, at high concentrations of oxygen vacancies the  $^1S$  states will be distributed in energy and some hybridized with the band resulting in metallic conduction at room temperature. The conductivity increase at 40°K is still observed as electrons from localized states are transferred to  $^3S$  delocalized states whose energy has been reduced by the ferromagnetic order. The conductivity minimum at  $T_c$  is similar to that found in degenerate Gd-doped EuO and is presumably due to critical scattering.<sup>30</sup>

Density of States: Von Molnar and Kasuya<sup>25</sup> have discussed how the conductivity of europium chalcogenides changes from semiconducting to metallic with increasing Gd doping: note particularly their Fig. 5. At first the Gd donors

are isolated and conduction occurs by thermal activation of carriers from the donors to the band. For heavy Gd doping, the random potential fluctuations cause a large tail to form on the conduction band which merges with broadened donor states. The result is a Fermi level above the mobility edge and metallic-type conduction. Much the same effect occurs with oxygen vacancy donors. At low concentrations, Region IV, the oxygen vacancy levels lie about 0.3 eV below the mobility edge. At higher concentrations, Region V, the donor levels have merged with the conducting states leaving the Fermi level above the mobility edge. As shown elsewhere,<sup>7</sup> the insulator-metal transition in sample IV-5 may be characterized by the 0.3 eV activation energy decreasing to zero as the magnetization increases below  $T_c$ . Apparently in sample IV-1, with fewer oxygen vacancies, the mobility edge lies higher and the activation energy, though decreased by increasing magnetization, is not driven to zero. The result is that conduction is still thermally activated at low temperature. Von Molnar<sup>31</sup> has found that his low temperature data<sup>28</sup> are consistent with Mott's<sup>32</sup> model of variable range hopping - that is,  $\log \sigma/\sigma_0 = -(T_0/T)^{1/4}$ .

In Regions I and II, since Eu<sup>3+</sup> ions are present, there are holes in the  $4f^7$  states and the Fermi level must be pinned at this level. The observed activation energies (0.45 to 0.7 eV) measure an average over the thermal equilibrium, energy dependent density of states, and mobility, weighted by the Fermi function. Only if there is a sharp mobility edge or band edge, is this activation energy the separation of the edge from the  $4f^7$  states. It is interesting to contrast these activation energies with the observed 1.1 eV edge of the  $4f^7-4f^6\ 5d$  optical absorption.<sup>5</sup> There are a number of possible sources for this difference. For instance, the lowest conducting states may come from either impurities or the 6s-band, which may lie below the 5d-band.<sup>23</sup> Furthermore, the final state of the optical absorption is probably a nonequilibrium state. For example, in EuS

and EuSe there is a shift in the luminescence maximum of about 1 eV down from the first maximum in the optical absorption spectrum.<sup>34</sup> Although the EuO luminescence was not measured below 1 eV it appears that the upper edge of the luminescence also shifts down by about 1 eV. These shifts are probably due to Frank-Condon type relaxation of the lattice and spin systems around the excited ion. In summary, the activation energy is an average over an equilibrium density of states, weighted by an energy dependent mobility and a thermal factor, while the optical absorption is an average over a nonequilibrium density of states, weighted by an oscillator strength.

The results of this work are consistent in some, but not all, respects to that of Oliver, et al.<sup>6</sup> They have classified their samples into two types. Type A samples were grown with excess Eu and show some kind of conductivity minimum near  $T_c$ . Type B samples show no conductivity change near  $T_c$  and are grown from stoichiometric amounts of starting material. The type A samples, which they are primarily concerned with, are similar to our Regions IV and V samples. Two type B, as-grown samples are reported, one with conductivity  $\sim 10^{-2}$  ( $\Omega\text{-cm}$ )<sup>-1</sup> constant in temperature and another with room temperature  $\sigma \sim 10^{-4}$  ( $\Omega\text{-cm}$ )<sup>-1</sup> decreasing to  $10^{-5}$  ( $\Omega\text{-cm}$ )<sup>-1</sup> at about 80°K, that is with a very small activation energy compared with our results. We have not found crystals of Type B. In our work we have found that stoichiometric starting composition leads to Region I behavior. Oliver, et al., report annealing a sample of  $\sigma < 10^{-8}$  ( $\Omega\text{-cm}$ )<sup>-1</sup> in an oxygen containing atmosphere at 1400°C and getting type B behavior and annealing in Eu at 1400 and getting type A. The Eu anneal is consistent with our picture. Possibly the conduction in type B material is dominated by filaments of  $\text{Eu}_3\text{O}_4$  whereas in our Region I sample the  $\text{Eu}_3\text{O}_4$  precipitates are isolated grains and conduction is determined by the EuO host.

Curie Temperature: Initial permeability measurements have shown that

samples from all regions have Curie temperatures within a degree of 69.3°K. This result is particularly noteworthy since Curie temperatures up to 135°K have been observed for metallic Gd-doped EuO crystals.<sup>9</sup> Specifically, Von Molnar and Shafer<sup>30</sup> have observed  $T_c = 123^{\circ}\text{K}$  for a metallic sample of 2% Gd-doped EuO with 0.7% carriers per Eu site. Kaldis, Schoenes, and Wachter<sup>35</sup> have observed  $T_c = 85^{\circ}\text{K}$  for a semiconducting sample of 0.66% Gd-doped EuO with 0.03% carriers just above  $T_c$ . Our sample, V-2, which showed no  $T_c$  increase was metallic with 0.03% carriers above  $T_c$ . The fact that we observe no increase may be due to the low carrier concentration or to the difference between doping with Gd or excess Eu.

#### 2.4 Summary and Conclusion

We have systematically correlated a wide range of physical properties of EuO crystals with the parameters of crystal growth. We have used the physical properties together with quenching experiments to determine a new phase diagram which in turn may be used as a guide to grow crystals with the desired composition or physical properties. The major features of the phase diagram are as follows: at the melting point (1965 °C) only nonstoichiometric oxygen-rich EuO exists; the variations in the EuO composition are about 2-4%, more on the oxygen-rich side; crystals of EuO may be grown at considerably lower temperature than was previously known, the final EuO composition may be controlled by controlling the growth temperature. Two methods of crystal growth were used in these experiments: a single crucible method in which the EuO crystal was in contact with the Eu-rich liquid; and a two crucible method in which the EuO was in contact only with Eu vapor. Both oxygen- and Eu-rich crystals could be grown by either method. Crystals grown by the second method were generally more sound. Crystals of varying composition were classified into five categories according to their physical properties, and are summarized in Table II. The oxygen-rich samples were characterized, from the infrared spectra, by the presence of  $\text{Eu}_3\text{O}_4$  as a

second phase and by Eu<sup>3+</sup> in solid solution. On increasing the Eu-metal in the starting composition the infrared absorption decreased and then increased with a different spectrum. The minimum absorption is presumed to correspond to stoichiometric EuO. The new absorption is then due to excess europium, probably in the form of oxygen-vacancies. Oxygen-rich samples have activation energies for conduction in the range 0.45-0.7 eV. On the Eu-rich side there is a lower (0.3 eV) activation energy which presumably corresponds to donor oxygen-vacancies. These crystals have an insulator-metal transition below the ferromagnetic ordering temperature. Crystals containing the largest Eu excess have large infrared absorption and metallic conductivity at all temperatures.

In conclusion, this work represents an example of the results which may be obtained from a systematic study of the correlation between physical measurements and crystal growth parameters. We have shown how physical measurements, infrared and conductivity in this case, are extremely valuable for detecting small deviations from stoichiometry. Correspondingly, these deviations must be understood in order to explain the resulting variations in the physical properties. In doped systems as well, such a study may be necessary in order to separate out the effects due to the dopant from those due to stoichiometry. These techniques should be applicable to many other systems where compounds with variable stoichiometry occur.

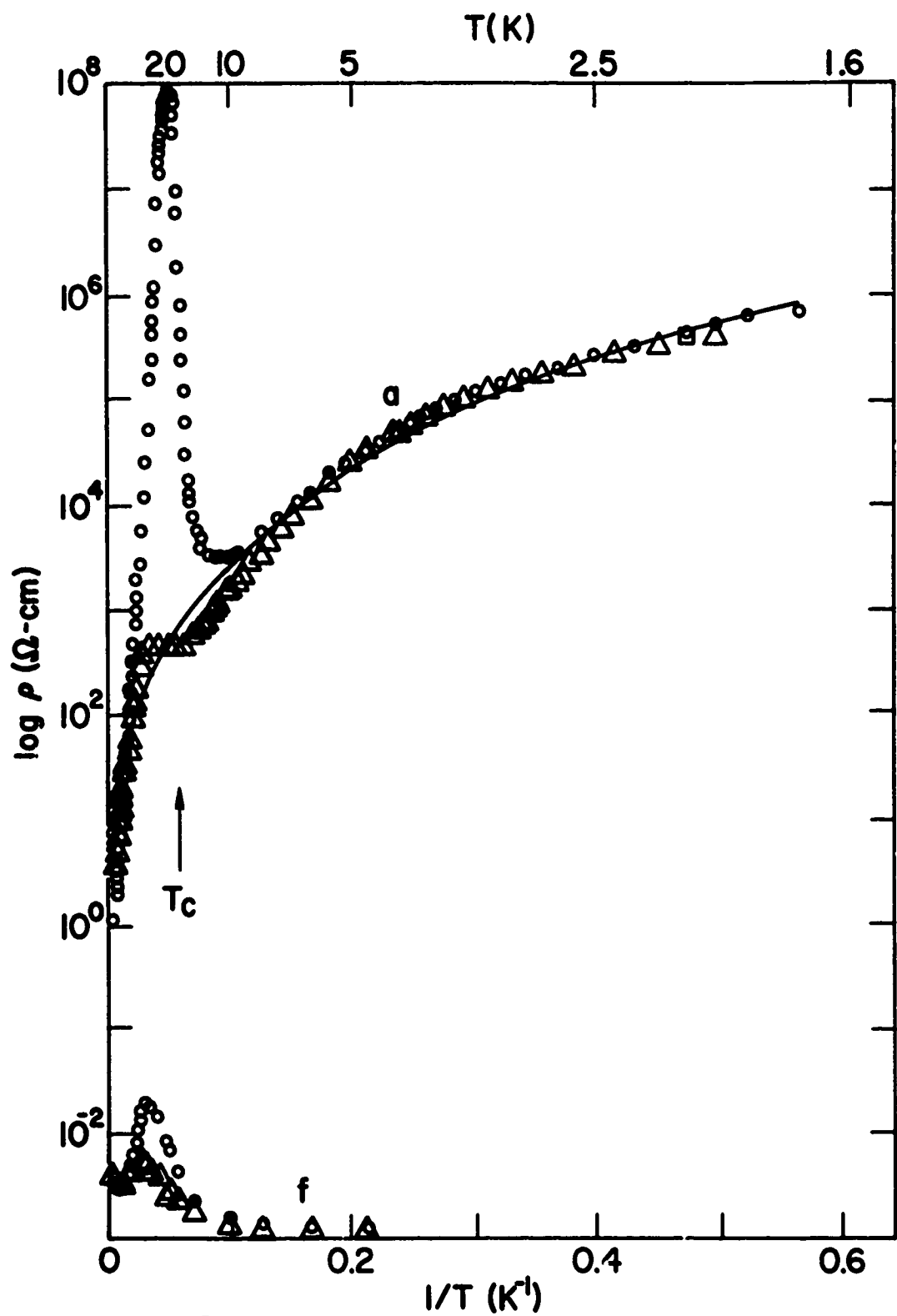


Figure 8.  $\log \rho$  vs  $1/T$  for  $H = 0$  (circles) and  $H = 32.8$  kOe and  $20$  kOe (triangles), respectively, for samples a and f. The solid line is a fit of  $\exp(T_c/T)^{1/4}$  to the data.

### 3.0 SYSTEMATICS OF CONDUCTION IN A BANL / AL: THE EuS SYSTEM

In this section we report transport measurements, on non-stoichiometric EuS, which afford considerable insight into the general phenomenon of non-metallic electronic conduction in disordered materials.<sup>36</sup> A series of n-type EuS single crystal samples was prepared in which carrier concentrations were varied from  $<10^{18}$  to  $10^{20} \text{ cm}^{-3}$  by slightly increasing the Eu/S ratio. In several samples thermally activated conduction is observed at both high and low temperatures but the activation energy decreases markedly as  $T \rightarrow 0$ , suggesting that some form of variable-range hopping conduction (ref. 36, p. 41) dominates at low temperatures.

All samples exhibit large, magnetic field-dependent resistivity peaks at their ferromagnetic ordering temperatures, such as those shown in Fig. 8, which shows resistivity data for the most and least conducting samples. These peaks are quenched by a magnetic field (see Fig. 8), are similar to previously studied peaks,<sup>37,38</sup> and will not be discussed here. Rather we shall consider the results, outside the range  $T_c/2$  to  $2T_c$ , where the magnetoresistance was found to be small.

Samples studied cover the transition between metallic and non-metallic conduction in this system. In Fig. 8, the least doped sample, a, shows thermally activated conduction both above 40K and below 10K, while the most doped sample, f, does not show thermal activation at either extreme. Fig. 9 presents the high-temperature data, resistivity and Hall coefficient, for all samples. These data may be described approximately by the expressions  $\rho = \rho_\infty \exp(\Delta_\rho/kT)$  and  $R = R_\infty \exp(\Delta_H/kT)$ . Table IV lists experimental parameters obtained in this way. Systematic trends are evident in both activation energies and in the prefactors. The resistivity activation energy,

$\Delta_p$ , decreases from 28.5 mV for sample a to 0 for sample f, while  $N_H \equiv 1/R_e$  increases over two decades. Both the Hall activation energy  $\Delta_H$  and the ratio  $\Delta_H/\Delta_p$  decrease as well.

It proves impossible to reconcile the high temperature resistivities and Hall data with a description of conduction by activation from donor states to the bottom of a well-defined conduction band. We shall show, instead, that these data are consistent with a model in which random potential fluctuations smear the conduction band edge into a small (12 mV) exponential tail. Random potential fluctuations are associated both with defects present in all samples and with defects, such as sulfur vacancies, which are associated with the changing stoichiometry and electron concentration. Our numerical calculations show that to fit the data, the band tail must be more-or-less independent of stoichiometry. Consequently, we have used a "rigid band" approximation, and assume that the band reaches deeper than the donor levels so that it simply fills up with increasing doping. About 400 ppm of oxygen are found in all our samples, which may account for this rigid band tail. Following Kane<sup>39</sup> we shall describe the conduction band tail by assuming that scattering from random arrangements of defects shifts the low-lying states rigidly, and characterize the result by a probability distribution,  $P(E)$ , of the energy of the spatially-varying band edge. The density of states is then

$$n(E) = \int_{-\infty}^E dE' P(E') n_0(E-E'), \quad (3.1.1)$$

where  $n_0$  is the density of states in a simple parabolic band. The probability function,  $P(E) = (1/2E_0) \exp(-|E'|/E_0)$  was used for calculations with (3.1.1), as it gave better agreement with our data than did the Gaussian derived by Kane.

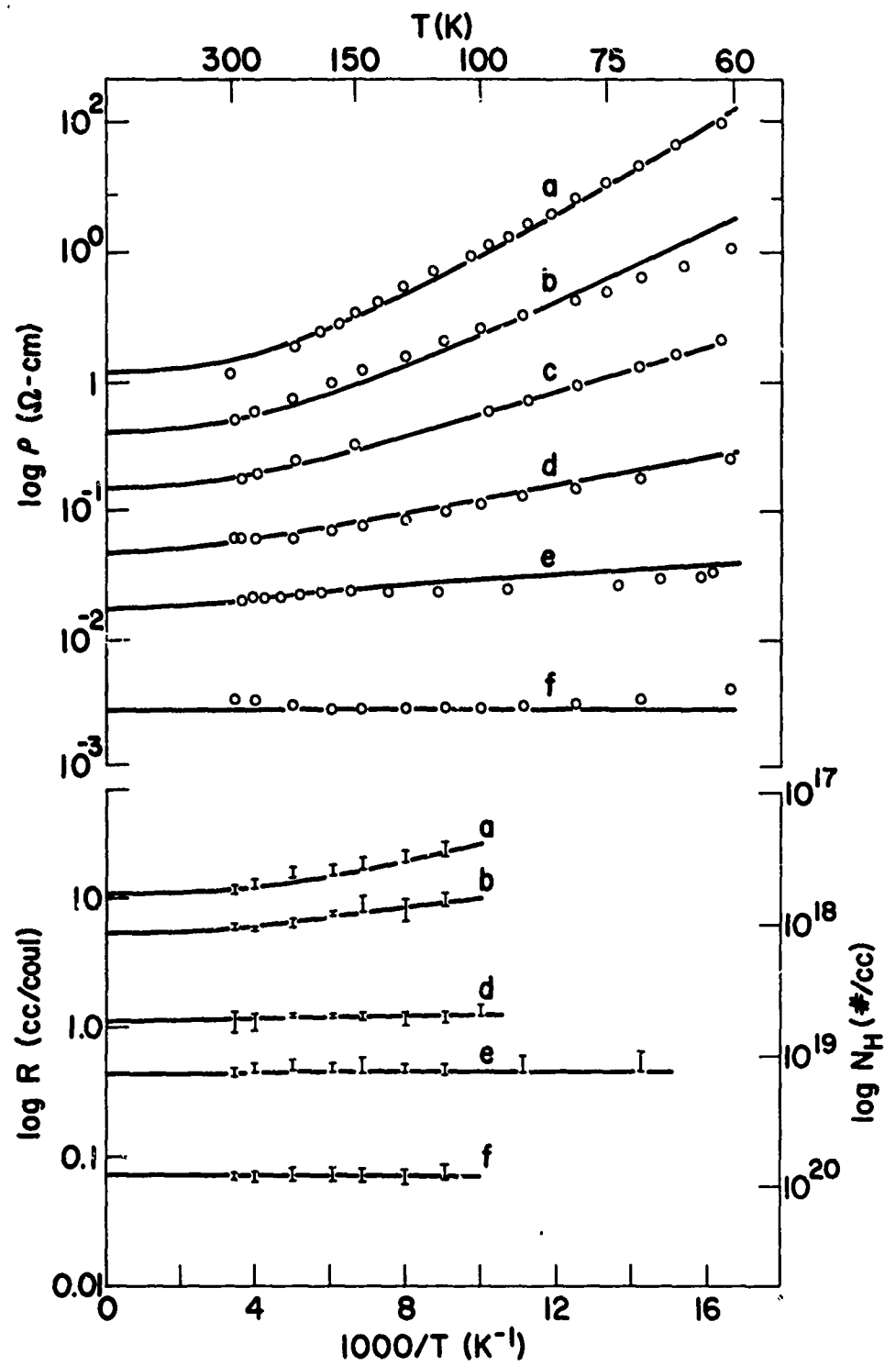


Figure 9. (a)  $\log \rho$  vs  $1/T$ , (b)  $\log R$  (Hall constant) and  $N_H \equiv 1/Re$  vs  $1/T$ .

Defect scattering also gives rise to a strong energy dependence of the electron mobility, since carriers are excluded from regions in which their energy is less than the energy of the local band edge.<sup>40</sup> At high temperatures, thermally assisted tunneling through the forbidden regions will dominate conduction in the band. The following high temperature expression for the mobility,  $\mu(E)$ , was chosen to reflect these two physical effects:

$$\begin{aligned} \mu(E) &= \mu_0 & E > E_M; \\ &= \mu_0 \exp((E-E_M)/kT) & E < E_M. \end{aligned} \quad (3.1.2)$$

$E_M$  is similar to the "mobility shoulder" of Mott (ref. 36, p. 43ff) and lies above the zero temperature mobility edge discussed in Ref. 40. Redfield<sup>41</sup> has proposed a similar soft mobility edge. The temperature dependence assumed in (3.1.2) has been suggested by Cutler and Mott<sup>42</sup> as a consequence of thermal emission over potential barriers. The temperature dependence appears to be necessary to give a fit to our data. The systematic features of the data may be explained from the model without further specification of parameters. If the zero temperature Fermi level,  $E_F(0)$ , in a sample lies well below  $E_M$ , then as  $T$  increases, electrons fill states at higher energies, with higher mobilities, and the resistivity decreases. If  $E_F(0)$  exceeds  $E_M$ , the resistivity will be non-activated. This behavior is seen in Fig. 9a, where the greatest temperature dependence ( $\Delta_p$ ) occurs for the sample with the smallest number of carriers (i.e., lowest  $E_F(0)$ ), and  $\Delta_p \rightarrow 0$  for the heavier doped samples.

At very low temperatures, in those samples where  $E_F(0)$  is well below  $E_M$ , hopping between localized or nearly-localized states should dominate the

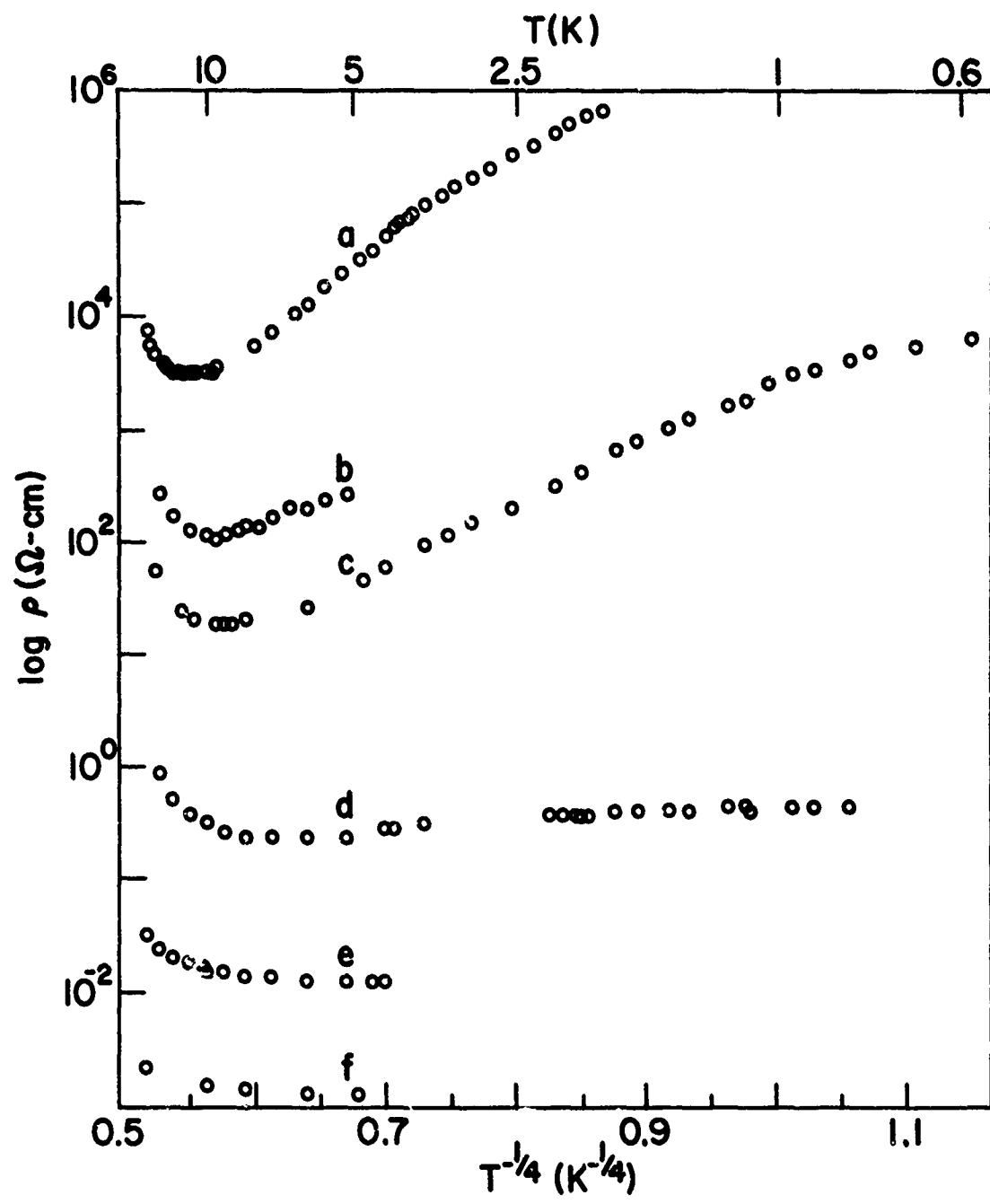


Figure 10.  $\log \rho$  vs  $T^{-1/4}$ .

conduction process. The relation proposed by Mott for variable-range hopping,  $\rho = \rho_0 \exp(T_0/T)^{1/4}$ , may describe this limit. A plot of our low-temperature data against  $T^{-1/4}$  (Fig. 10) shows several cases which are reasonably well described by this equation. The parameter  $T_0$  may be expressed as<sup>43</sup>

$$T_0 = 4v_c \alpha^3 / n(E_F) \quad (3.1.3)$$

where  $v_c$  is a constant of order 1, and  $\alpha^{-1}$  is the range of a localized state wave function. Expression (3.1.3) was derived for a constant density of states, but corrections to it due to the exponential variation of our  $n(E)$  can be shown to be modest.<sup>44</sup> For states deep in a conduction band tail, as  $E_F(0)$  decreases,  $n(E_F)$  and  $\alpha^{-1}$  also decrease, so  $T_0$  will increase. Sample a, the least conducting, shows the largest slope in Fig. 10, as expected in this picture.

The quantitative application of this model is illustrated in Fig. 11. Using a roll-off factor  $E_0 = 12$  meV in  $P(E)$ ,  $n(E)$  (solid line) was obtained from  $n_0(E)$  (dashed line). The effective mass in  $n_0$  was taken to be  $1.1 m_e$ , in agreement with independent experimental measurements.<sup>45</sup> The Fermi levels,  $E_F(T)$ , for the various samples are determined by conservation of the total number of electrons,  $N = \int_{-\infty}^{+\infty} dE n(E) f(E-E_F(T))$ , where  $f(E)$  is the Fermi function. Values of  $E_F(0)$  obtained in the course of our fitting procedure are indicated in Fig. 11 by a,b,c... (paramagnetic state) and a',b',c'... (ferromagnetic state).

The specification of  $E_M$  is related to that of  $P(E)$ , since  $E_M$  is the energy at which defect scattering becomes significant, and below which activated conduction is seen. For the calculations presented,  $E_M$  was set equal to  $E_0$ ,

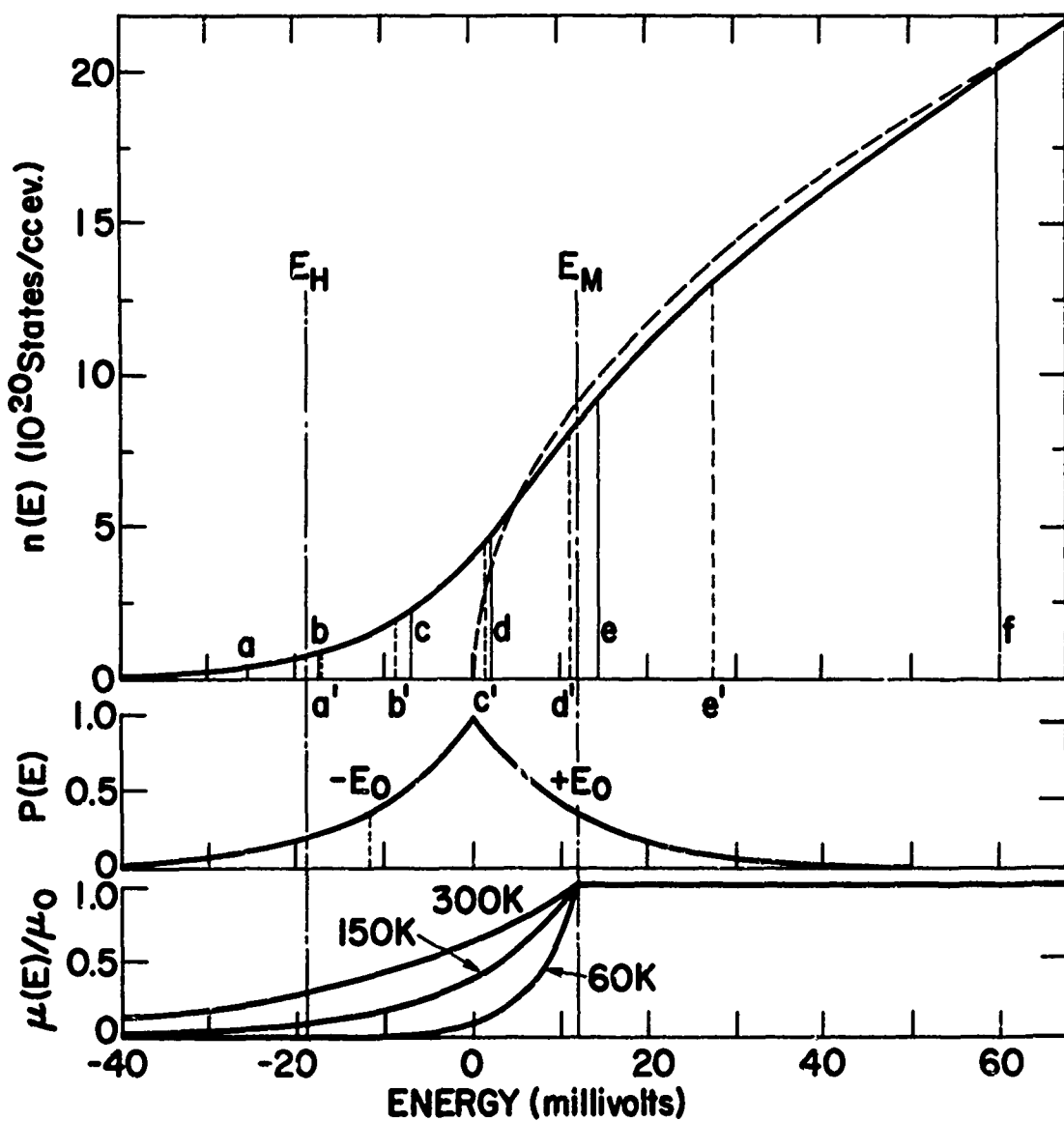


Figure 11. (a) Band tail density of states (solid) derived from unperturbed states (dashed) using the fluctuation probability distribution (b). (c) Normalized mobility vs energy.

at which energy fluctuations excluded roughly 1/6 of the sample volume. The resistivity was then calculated, using

$$1/\rho(T) = e \int_{-\infty}^{+\infty} dE n(E) f(E-E_F(T)) \mu(E). \quad (3.1.4)$$

We find that (3.1.4), with this choice of  $E_M$ , predicts an approximately exponential temperature dependence for  $\rho$  in the range 50-300°K with activation energy  $\Delta_\rho \sim 3/4 (E_M - E_F(0))$ . The calculations also show that at room temperature most of the carriers are at energies above  $E_M$  where  $\mu(E)$  is constant, so that  $R(300^\circ)$  gives a reliable index of the carrier concentration,  $N_T$ , and could be used to determine  $E_o$ . When the exponential form for  $P(E)$  is used in (3.1.1),  $N_T$  is approximately proportional to  $\exp(-E_F(0)/E_o)$ . Thus the experimental observation (Table IV) that both  $(R(300^\circ))^{-1}$  and  $1/\rho_\infty$  in the six samples were proportional to  $\exp(-\Delta_\rho/8.5 \text{ mV})$  gives  $E_o = 11 \text{ mV}$ , in substantial agreement with our final value of  $E_o = 12 \text{ mV}$  which gave the best fit.

Consideration of the temperature dependence of the Hall coefficient completes the specification of our model. Calculations of the Hall coefficient using small polaron models<sup>46</sup> yield the prediction  $\Delta_H = \frac{2\Delta_\rho}{3}$ , while, for conduction above a mobility edge, Friedman's recent Random Phase Model calculation<sup>47</sup> gives  $\Delta_H = \Delta_\rho$ . In both calculations the Hall mobility  $\mu_H \equiv R/\rho$ , is predicted to be less than  $0.1 \text{ cm}^2/\text{volt sec}$ . Since we observe that  $\Delta_H/\Delta_\rho$  is sample-dependent, and  $\mu_H \sim 20 \text{ cm}^2/\text{volt sec}$ . is comparable to the mobilities of much more metallic samples,<sup>37</sup> it appears that neither description applies here.

We find, instead, that the Hall effect can be described by the expression  $R = 1/N_H e$ , where  $N_H$  represents the number of electrons sufficiently mobile to feel a Lorentz force. As the simplest possible approximation, we introduce a

Table IV

Experimental values of transport data and theoretical estimates using  $E_0 = E_m = 12\text{mV}$ ,  $E_H = -19\text{mV}$  and  $m^* = 1.1m_0$ .

	$\rho$ 290 K $\Omega\text{-cm}$	$N_{\text{D}} \pm 1/\text{cm}^3$ 290 K	$\Delta_D$ exp. mV	$\Delta_D$ theo. mV	$\Delta_H$ exp. mV	$\Delta_H$ theo. mV	$v_0$ $\text{cm}^2/\text{v-s}$	$E_F$ 0K mV	$T_0^{1/4}$ exp. $^{\circ}\text{K}^{1/4}$	$T_0^{1/4}$ theo. $^{\circ}\text{K}^{1/4}$	$1/\lambda$ theo. $\text{A}$
a	1.1	$5.5 \times 10^{17}$	29	29	10.8	10.8	9	-25	19	36	11
b	0.51	$1.2 \times 10^{18}$	22	23	8.3	7.1	13	-17	--	27	13
c	0.17	---	16	16	-	-	15	-7	12	17	18
d	0.067	$5.5 \times 10^{18}$	9.9	10	1.3	1.5	22	+2	2	3.8	56
e	0.020	$1.4 \times 10^{19}$	2.6	4.3	0.7	0.4	25	+14	0	0	-
f	0.0034	$8.5 \times 10^{19}$	-	-	0	0	24	+60	0	0	-

lower cutoff parameter,  $E_H$ , and count only the states above  $E_H$  in  $N_H$ . Thus,

$$1/R_e \equiv N_H \equiv \int_{E_H}^{\infty} n(E) f(E-E_F(T)) dE. \quad (3.1.5)$$

The value chosen for  $E_H$ , shown in Fig. 11 was -19 mV.

The fitting procedure used to describe the high temperature data can be summarized as follows:  $E_M$ ,  $E_0$  and  $E_H$  are universal to all samples, and determined primarily by the systematic features of the data. They are not quite unique, but setting  $E_M = E_0$  resolves this ambiguity. The total carrier concentrations (and hence the  $E_F(0)$ 's plotted in Fig. 11) were determined for each sample by fitting  $R(290K)$  with (3.1.5). The Hall coefficient,  $R(T)$  (solid lines of Fig. 9b), and the activation energies  $\Delta_H$ ,  $\Delta_p$  (Table IV), can be predicted from the model with no further parameters. A value of  $\mu_0$  was chosen for each sample to normalize the theoretical curves of  $\rho(T)$  (solid lines) plotted in Fig. 9a. Values of  $\mu_0$ , given in Table IV, were found to increase with increasing conductivity of the samples. Agreement of the data (Fig. 9, Table IV) with predictions of the model is quite good.

The high temperature data completely determines the model. We next use it to predict the behavior of our samples in the low temperature (hopping) regime. The slope of the data plotted in Fig. 10 increases for samples with fewer and more tightly localized electrons as noted above. Sample d, which is seen in Fig. 10 to approach non-activated behavior, is also the sample in which  $E_F(0)$  (ferromagnetic) falls slightly below  $E_M$ . Samples e and f with  $E_F(0)$ 's above  $E_M$  show no activation.

Quantitative predictions are possible, using (3.1.3), if the tunneling range,  $\alpha^{-1}$ , for a state at  $E_F$ , is known. Taking  $E_0$  as the average energy for

the top of a potential fluctuation,  $\alpha$  can be obtained from the WKB relation,

$$\alpha(E_F(0)) = (2m^* (E_0 - E_F(0))/\hbar^2)^{1/2}. \quad (3.1.6)$$

Predicted values of  $T_0^{1/4}$ , calculated from (3.1.3) and (3.1.6) with the ferromagnetic  $E_F(0)$ 's and  $v_c = 4$ ,<sup>43</sup> are compared in Table IV with values of  $T_0$  defined by the average slopes of the data in Fig. 10. The calculated values of  $T_0^{1/4}$  all lie within a factor of two above the observed values. Since (3.1.6), which describes rectangular barriers, probably gives too large a rate of decay for wave function tunneling through the forbidden regions, we feel this agreement is excellent, and the overestimate understandable.

In conclusion, we have observed systematic trends in the parameters characterizing transport in a series of EuS crystals of varying stoichiometry. These trends suggest that conduction occurs in and above a conduction band tail caused by random potential fluctuations. A quantitative model which includes an energy and temperature dependent mobility in the band tail has been used to explain the systematic changes between samples, and to relate the high temperature (activated) conduction to the variable range hopping seen at low temperature. The Hall data was understood in this model by assuming that the more localized electrons ( $E < E_H$ ) do not contribute to the Hall current.

4.0 THE MAGNETIC SEMICONDUCTOR  $Gd_{3-x}v_xS_4$ 4.1 Introduction

Although both transport and magnetic measurements have been reported on various rare earth  $Th_3P_4$ -type structures,<sup>48</sup> to the best of our knowledge only very few examples of systematic studies on either of these properties exist. Interest in these substances is twofold: first of all the  $Re_{3-x}v_xX_4$  ( $X = S, Se, Te$ ) ( $0 \leq x \leq 1/3$ ) change continuously from metals to insulators with increasing vacancy ( $v$ ) concentration,  $x$ , leading to a variety of cooperative effects such as superconductivity and ferromagnetism;<sup>48</sup> secondly, as was first recognized by the authors of Ref. 49, the random distribution of vacancies at the Th sites leads to fluctuating repulsive potentials and tailing of the conduction band in which the electronic states are localized. The purpose of this section is to present magnetic and transport measurements on magnetic  $Gd_{3-x}v_xS_4$  and to interpret them, in part, in terms of the concepts developed by Cutler and Mott<sup>49</sup> for paramagnetic  $Ce_{3-x}v_xS_4$ .

4.2 Experimental

Crystals were grown from previously synthesized compositions in sealed W crucibles by heating to the melting point and cooling slowly to room temperature. The resulting material does not show any easy direction for cleavage and magnetic measurements were performed on small samples of arbitrary shape. D.C. transport measurements, however, were made on crystals shaped as rectangular parallelopipeds.

Results of magnetic measurements thus far obtained are summarized in Fig. 12. Although we do not have an independent measure of the concentration at this time, the systematic change in the magnetization data is related to the

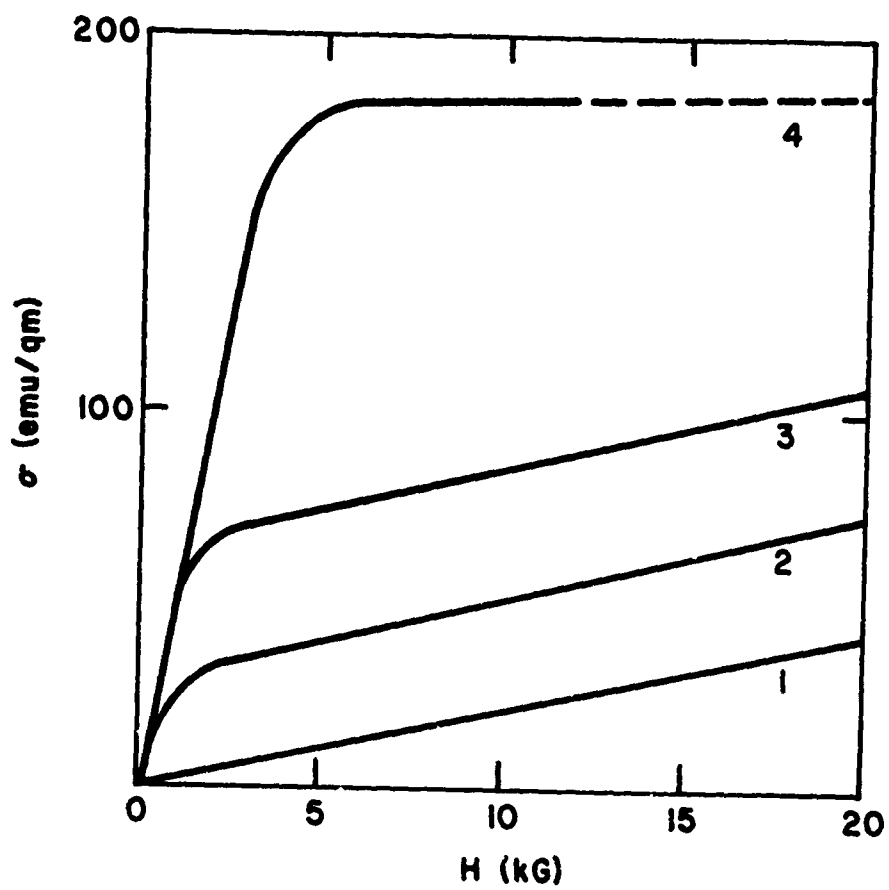


Figure 12. Magnetization curves for  $\text{Gd}_{3-x}\text{V}_x\text{S}_4$  at 4.2°K. Samples have increasing Gd concentration starting with  $x = 1/3$  for sample 1. The exact values of  $x$  have not been determined.

nominal concentration of the charge used for crystal growth. Figure 12 demonstrates that there is an increase in the saturation magnetic moment as the gadolinium concentration is increased from sample 1 to 4. In this system, for  $x$  equals 1/3, the end member concentration is  $\text{Gd}_2\text{S}_3$ , a valence compound and an insulator, having the maximum vacancy concentration. The linear dependence of magnetization with field for  $\text{Gd}_2\text{S}_3$  is shown in Fig. 12 for sample 1, indicating that the insulating composition is antiferromagnetic. An increase in gadolinium (or electron concentration) results in the appearance of ferromagnetism. In the intermediate composition range the spontaneous zero field moments of samples 2 and 3 are of the order of 30 and 60 emu/g respectively. If all the Gd moments were aligned, the saturation value would be about 190 emu/gm as in sample 4. It is interesting that the slope of the linear parts of curves 2 and 3 are essentially the same as the slope for the antiferromagnetic  $\text{Gd}_2\text{S}_3$ .

In attempting to interpret this data we can rule out ferrimagnetism because above  $T_c$  the temperature-susceptibility curves follow the Curie Weiss law and do not show the Neel hyperbola characteristic of ferrimagnetism. Although several models suggest themselves, from the magnetic data alone we can only speculate on the nature of the magnetic structure. One of the more satisfying models would invoke a spiral configuration with the antiferromagnetic end member having the spins aligned perpendicular to the axis of the spiral. As conduction electrons are added the increased exchange would tilt the spins toward the spiral axis giving rise to a ferromagnetic component.<sup>50</sup> In projection there is then a cone having an angle varying from 180 to 0° and the magnetization would vary from antiferromagnetism to the fully saturated ferromagnetism observed for sample 4. Although gadolinium is

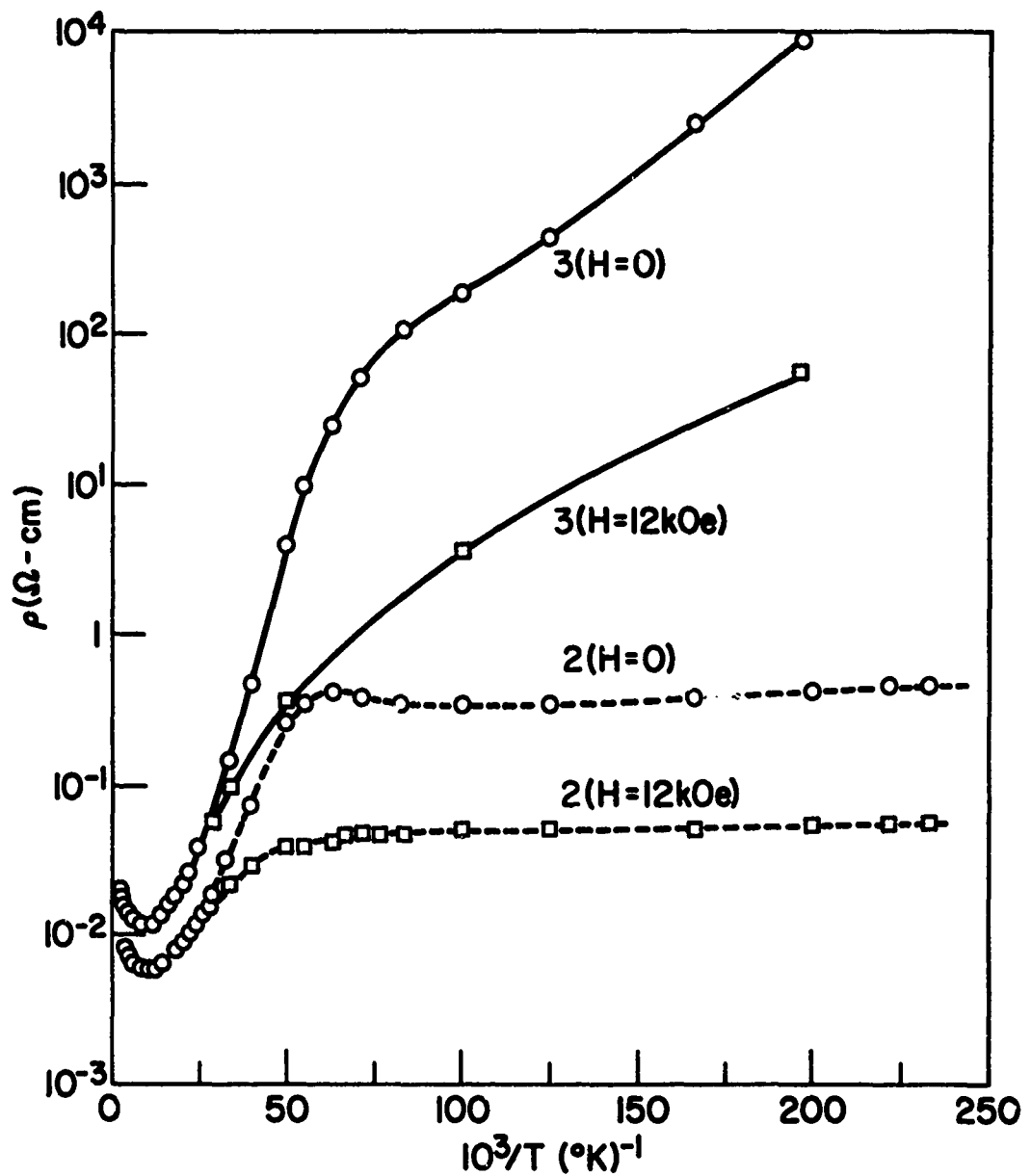


Figure 13. Resistivity,  $\rho$ , vs reciprocal temperature. The paramagnetic Curie temperatures are  $\theta(3) = 16.1^\circ\text{K}$  and  $\theta(2) = 22.2^\circ\text{K}$ .

an unfavorable element for neutron defraction (because of its enormous cross section) we have been exploring the possibility of determining the magnetic structure using neutron diffraction techniques.

Our present investigation of transport in the  $Gd_{3-x}V_xS_4$  system includes only samples 2 and 3. The results of the resistivity,  $\rho$ , with and without an applied field of 12 kOe as a function of temperature are exhibited in Fig. 13. The following features should be noted: (i) Both samples show a resistance minimum near 100°K; (ii) Between  $\sim 100^{\circ}\text{K}$  and  $\sim \theta$ ,  $\rho$  is activated with an energy  $E(3) \sim 1.7 \times 10^{-2} \text{ eV}$  and  $E(2) \sim 1.1 \times 10^{-2} \text{ eV}$ . Below  $\theta$ ,  $\rho$  remains activated but with a significantly reduced activation energy; (iii) Application of a magnetic field reduces  $\rho$  and  $E$  below  $\sim 40^{\circ}\text{K}$ . It is clear that the negative magnetoresistance which is effected either by an applied magnetic field or by temperature (through the Weiss field), is related to the state of magnetic order.

Figure 14 depicts the results of thermoelectric power and Hall measurements. The Seebeck coefficient,  $S$ , has a minimum near 100°K, just as did  $\rho$ , rises to a maximum just above  $\theta$ , and then decreases towards 0 as  $T \rightarrow 0$ . The sign of  $S$  is always negative. The Hall coefficient,  $e_H/H_A$ , is negative at room temperature but reverses sign near, but below, the temperature at which  $\rho$  is a minimum. For reasons discussed below, this sign reversal was unexpected and we have attempted to eliminate such spurious causes for anomalous Hall behavior as surface effects<sup>51</sup> and an unusually large Nernst-Ettinghausen effect. The former was tested by comparing the temperature dependent resistivities of samples with clean and lapped surfaces. No significant differences were observed. The latter was tested by comparing 210 Hz and D.C. results<sup>52</sup> on sample 2 at 300°K and  $\sim 56^{\circ}\text{K}$ . Both the

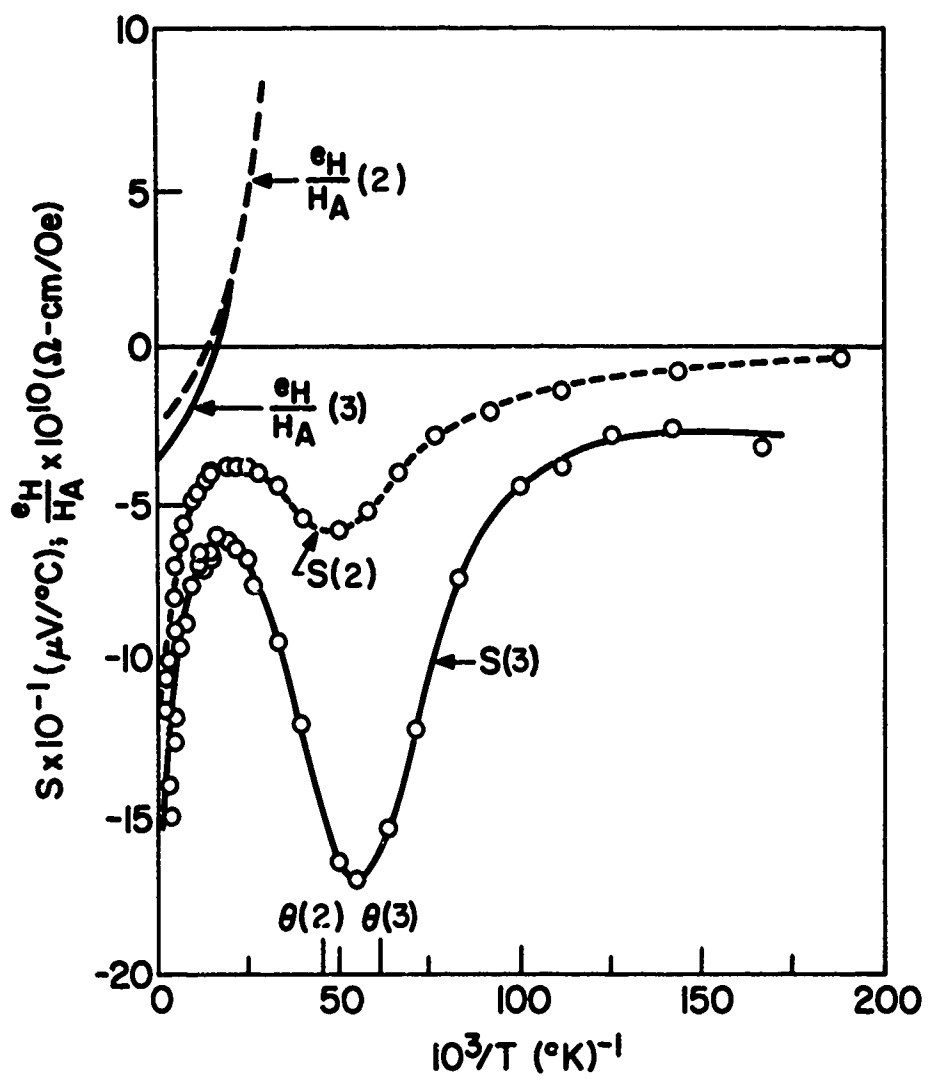


Figure 14. Hall coefficient,  $e_H/H_A$  and Seebeck coefficient,  $S$ , vs reciprocal temperature.

magnitude and sign of the Hall coefficient agreed. We were unable to make Hall measurements below  $\sim 35^{\circ}\text{K}$  because the onset of the large negative magnetoresistance masked the effect.

#### 4.3 Discussion

If we restrict our discussion to the region above  $\theta$ ,  $\text{Gd}_{3-x}^v \text{S}_x^4$  exhibits resistivity characteristics (Fig. 13) very similar to those observed in  $\text{Ce}_{3-x}^v \text{S}_x^4$ .<sup>49</sup> Cutler and Mott<sup>49</sup> analyze their data in terms of band conduction above the mobility edge at high temperatures and hopping conduction in localized states below this edge at low temperatures. The potential giving rise to this tail is attributed to the disordered vacancies in the  $\text{Th}_3\text{P}_4$  structure. Besides the resistivity minimum in various samples of  $\text{Ce}_{3-x}^v \text{S}_x^4$ , with  $x$  near 1/3, we note other similarities in transport phenomena.  $|S|$  decreases linearly with decreasing  $T$  with a slope having non-zero intercept but in several cases starts to rise again in a manner similar to that shown in Fig. 14 below  $\sim 100^{\circ}\text{K}$ . The sign of  $S$  is always negative. Cutler and Mott<sup>49</sup> argue that hopping transport results in a linear dependence of  $S$  on  $T$ , i.e.

$$S = C_1 + C_2 T, \quad (4.3.1)$$

where  $C_1$  and  $C_2$  are constants, provided that the density of states at the Fermi energy,  $N(E_F)$ , and  $\sigma(E_F) = 1/\rho(E_F)$  are appreciable. If this is not the case, these authors show that an increase in  $|S|$  is expected, since transport will then be dominated by contribution of thermally excited electrons above

the mobility edge.  $S$ , as well as  $e_H/H_A$  are negative as expected, since the substitution of Ce atoms for vacancies adds electrons to the conduction band.

Since transport in the paramagnetic  $\text{Ce}_{3-x} \text{V}_x \text{S}_4$  system is satisfactorily explained in terms of localization of electron states, we shall adopt a similar point of view for its ferromagnetic counterpart  $\text{Gd}_{3-x} \text{V}_x \text{S}_4$ , with the additional hypothesis that at least part of the energy which localizes the electrons is magnetic in origin. The idea of localization through exchange interactions,  $J_{c-f}$ , between conduction electrons and localized spins has been explored in detail with respect to the transport properties of NaCl-type Eu chalcogenides.<sup>53</sup> We wish to note here only two properties of this magnetic binding energy,  $E_m$ : (i)  $E_m$  exists far above the magnetic ordering temperature because  $J_{c-f}$  is, in general, larger than  $J_{f-f}$ , the exchange primarily responsible for long range order; (ii)  $E_m$  approaches 0 with increasing magnetic order since  $J_{c-f}$  can no longer significantly alter the magnetic environment near the electron.

The gross features of the temperature dependence of the resistivity in samples 3 and 2 can then be explained as follows: (i) the approximately linear decrease in  $\rho$  between 300 and 100°K is dominated by lattice scattering of thermally excited band electrons; (ii) the activated process between  $\sim 80$  and  $\sim 20$ °K is dominated by hopping in localized states (although thermally excited states may contribute); (iii) near and below  $\theta$ , the activation energy for transport becomes smaller due to the onset of magnetic order, as seen in Fig. 13 below  $\sim 20$ °K. The qualitative behavior with an applied magnetic field follows, since the magnetic field tends to decrease the binding energy for the electron and hence its activation energy.

The model is also consistent with the observed behavior of  $S$  if we accept the explanation for the low temperature rise in  $|S|$  given by Cutler and Mott,<sup>49</sup> i.e. that  $S$  is dominated by contributions from band states. The final reduction in  $|S|$  below  $\theta$  is then due to the reduction in magnetic binding energy which will increase the number of thermally excited carriers. Furthermore, fundamental considerations require that  $S$  approach 0 at  $T \rightarrow 0^{\circ}\text{K}$ .

We believe that the sign reversal of the Hall effect is due to a contribution from the anomalous Hall constant,  $R_1$ , usually found in ferromagnetic materials. A plot of  $e_H/H_A$  versus  $\chi$  for sample 2 (where the best data is available) yields a straight line with slope  $|R| \approx 7 \times 10^{-8} \Omega\text{cm}/\text{G}$  which is comparable in magnitude to values found in ferrites<sup>54</sup> where conduction is believed to occur in narrow d-bands. Further work is necessary to confirm this explanation but preliminary results, extrapolating to  $\chi = 0$ , yield electron concentrations of  $(1.6 \pm .2) \times 10^{20} \text{ cm}^{-3}$  and  $(2.5 \pm .2) \times 10^{20} \text{ cm}^{-3}$  for samples 3 and 2 respectively.

5.0 THE METALLIC  $\text{Gd}_{\mathbf{x}}\text{Se}_{\mathbf{1-x}}$  SYSTEM5.1 Introduction

In a recent effort to establish the composition of the phase boundary of the lowest concentration  $x$  in  $\text{Gd}_{3-x}\text{Se}_x\text{S}_4$ , we discovered that the primary crystallization had a NaCl-type structure with a deep blue metallic color, the remaining phase being a eutectic composition of NaCl and the  $\text{Th}_3\text{P}_4$ -type defect structures. The blue, metallic phase had a smaller lattice constant than expected for  $\text{GdSe}$ . This implied that  $\text{GdSe}$  has a wide range of homogeneity extending considerably into the Se rich field. This result was not comparable with earlier work which suggested that  $\text{GdSe}$  was essentially stoichiometric with practically no range of solid solubility.<sup>55</sup>

The trivalent rare earth monosulfides and monoselenides are generally gold colored and are metallic because the extra electron not used in bond formation is believed to be in a band formed by 5d and 6s wave functions. The  $^8\text{S}_{7/2}$  ground state of  $\text{Gd}^{+++}$  has an atomic moment of  $7\mu_B$  and is, as a pure spin state, insensitive to lower order crystalline field splittings. The metallic rare earth gold colored phases are antiferromagnetic with large negative exchange interactions, e.g.  $\theta_{\text{GdSe}} \approx -135^\circ\text{K}$ . If there is a wide range of homogeneity extending to high Se concentrations, then the number of excess electrons (one per  $\text{Gd}$  for the stoichiometric composition) should be significantly reduced and this should reflect in changes in electrical and magnetic properties with perhaps less profound effects than those observed in the ferromagnetic semiconductors.

5.2 Experimental

As a means of studying the extent of solid solubility in the  $\text{GdSe}$  system a large charge of a Se rich composition was synthesized using the following

procedure: All materials were handled in a He purged dry box. Metallic Gd sponge obtained from the Lunex Corp. having a nominal 99.9 concentration and 99.999 Se from the United Mineral and Chemical Corp. were reacted by the vapor transport of Se to the gadolinium side of an evacuated and sealed dual chamber quartz reaction tube. This reaction was carried out at a maximum temperature of 600°C because at higher temperatures there was evidence of quartz attack. Transport was considered complete when the characteristic color of Se vapor disappeared. The product of this reaction is quite inhomogeneous. The entire charge was transferred to a large tungsten crucible which was covered and sealed by electron beam welding. The crucible was then heated to 1600°C in a vacuum heated RF furnace. The sample was powdered and chemical analysis gave the composition Gd<sub>.42</sub>Se<sub>.58</sub>. A series of samples developed from mixtures of this composition and pure Gd were used for crystal growth. Samples of approximately 6 grams were pressed into pellets which were sealed into 3/8 x 2 in. tungsten crucibles. Crystals were grown in an induction heated RF furnace using a 10<sup>-6</sup> torr vacuum to protect the crucible from surface reaction. Temperature measurement and control were achieved with an NBS calibrated L&N automatic optical pyrometer, surface temperature having been calibrated with a black body measurement obtained with the same geometry. Samples were heated to the melting point and cooled at about a degree per minute to 700°C at which point the power was turned off.

X-ray data were obtained with a Guinier focussing camera using Si as an internal standard. A least squares fit to the data gave a standard deviation of 0.001 Å.

In the Semiannual Report (30 June 1971 to 31 December 1971) we reported an attempt to establish a sample composition scale using microprobe analysis for

relative composition and wet chemical analysis to fix the absolute value of composition. At that time the Gd rich composition phase boundary had not been reached and from subsequent analysis it became evident that although relative concentrations were good to  $\sim 0.5\%$  the absolute scale was in error. Reevaluation of the data with information on the full range of solid solubility and improvement in microprobe resolution have led to a shift in the composition scale.

An AEI MS-7 double focussing solid state mass spectrometer was used for impurity analysis of the Gd metal and several single crystals of the selenide. Y and Ho were found in the 100-200 ppm range and Cu, Si, O, C and Na at the 100-300 ppm level. Synthesis and crystal growth of the selenide led to small increases in Na and Cu concentrations and considerable reduction in the C and O impurity levels. Since the small increase in Na and Cu concentrations (about 50 ppm) was not found to scale with Gd content, the effects of impurities on physical properties were considered to be negligible.

Magnetization data were obtained with a force balance in fields up to 20 Kilogauss in the temperature range 4.2°K to room temperature.

A Cary 14R spectrometer, modified with a reflectivity jig for 10° incidence was used for measuring the shift in reflectance spectra with composition. Instrumental corrections were obtained with an evaporated gold film standard.

A standard 5 probe D.C. technique was used to measure the resistivity as a function of temperature as well as the Hall effect, wherever possible. Measurements were limited to signals greater than  $10^{-7}$  volts.

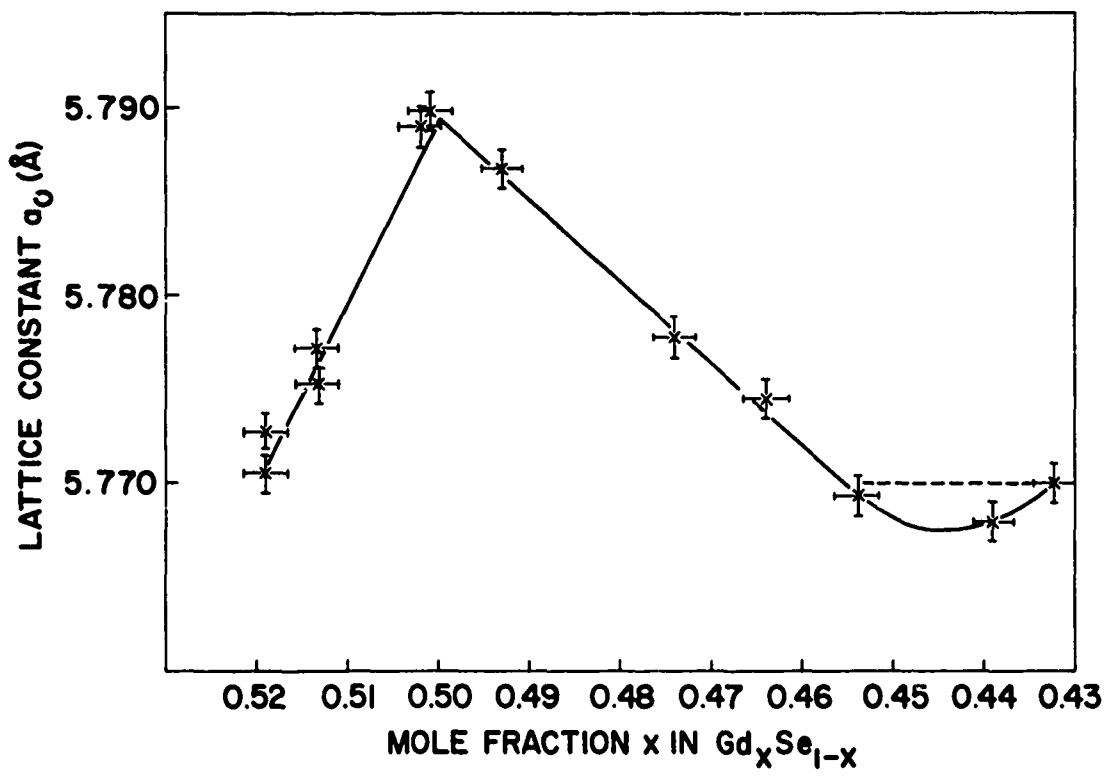


Figure 15. Lattice constant  $a_0$  as a function of composition  $x$  in  $\text{Gd}_x\text{Se}_{1-x}$ .

### 5.3 Results

A striking result of the crystal growth experiments is the dramatic variation of sample color as a function of composition. The Gd rich samples were a bright yellow gold color and as the Gd concentration decreased the color changed progressively to bronze, copper, red gold, purple and at the lowest Gd concentration, a deep metallic blue. Since there was a small temperature gradient along the crucible during crystal growth, a concentration gradient developed as the sample crystallized. Each single crystal ingot, therefore, graphically represented the crystallization process of the system. The initial crystallization was found to have the highest Gd concentration or most gold-like color and the final crystallization the lowest Gd concentration or most blue-like color, reflecting the range of solidus concentrations for a particular melt composition. Crystals of uniform color were cleaved from an ingot for analysis. The Gd rich compositions were found to melt at approximately  $1100^{\circ}\text{C}$ , reach a maximum of  $\sim 2350^{\circ}\text{C}$  with increasing Se concentration then decrease smoothly to about  $1750^{\circ}\text{C}$  for the blue, selenium rich phase.

A plot of lattice parameters as a function of concentration is shown in Fig. 15. The relative concentration given by microprobe analysis is good to 0.5% and error bars on the figure represent this uncertainty. Density determinations on samples falling on the linear portion of the curve in the Se rich region indicate that the lattice parameter decrease is associated with cation vacancies. Since we do not as yet have density data on Gd rich samples, we assume that the lattice parameter decrease in this region is associated with anion vacancies. The absolute concentration of the system was then deduced on the basis of the assumption that the two linear branches of the curve extrapolate to the stoichiometric composition, GdSe, with  $a_0 = 5.789 \text{ \AA}$ .

In the composition range  $x = .432$  to  $.453$  the lattice parameter goes through a minimum. The lattice parameter for the blue phase ( $x = 0.432$ ) is  $5.770 \text{ \AA}$ , which is identical with the value obtained from the NaCl pattern of the eutectic region. This composition, therefore, represents the phase boundary of the Se rich field.

Although there is some uncertainty concerning the absolute composition scale in Fig. 15 we have clearly established the existance of a wide range of homogeneity in the GdSe system. Guittard and Flahaut<sup>55</sup> (G and F) on the other hand, find GdSe to be an essentially stoichiometric compound with a lattice parameter  $a_0 = 5.765 \text{ \AA}$ . One possible reason for the differences in results may relate to the thermal treatment used in the two studies. G and F did not use temperatures above  $1450^\circ$  in preparing the selenide, whereas in this work the materials were all melted. Perhaps a long term lower temperature anneal would result in exsolution and the formation of the stoichiometric compound. G and F do observe a range of homogeneity in the heavier trivalent rare earth monoselenides starting with HoSe. In this case, however, they find a new phase in the vicinity of  $\text{HoSe}_{1.2}$  with a NaCl superstructure. The GdSe solid solution system does not show any evidence of superlattice formation.

The results of the resistivity measurements can be summarized as follows:

- (i) The bronze and gold colored samples, which have comparably low resistivities,  $\rho$ , exhibit a temperature dependence in  $\rho$  normal for magnetically ordered metals (lower curves in Fig. 16). The resistivity is linear in the paramagnetic region with a knee near  $T_N$  and drops precipitously as the temperature decreases towards  $0^\circ\text{K}$ . This is readily analyzed with three

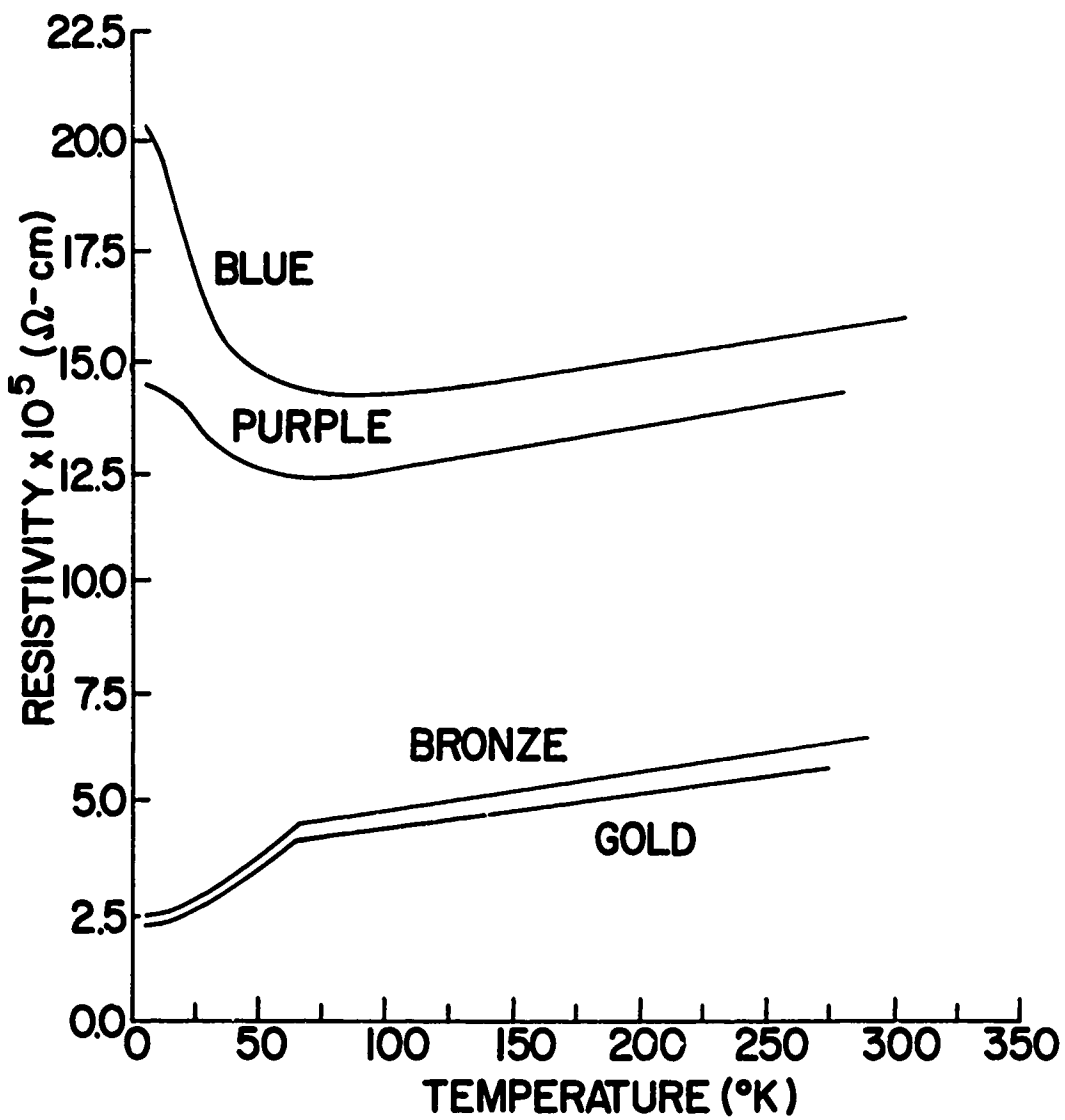


Figure 16. Resistivity,  $\rho$ , as a function of temperature ( $^{\circ}\text{K}$ ) for four compositions,  $x$ , in the  $\text{Gd}_x\text{Se}_{1-x}$  system.

## contributions to the resistivity

$$\rho = \rho_L + \rho_i + \rho_m \quad (5.3.1)$$

where  $\rho_L$  = lattice,  $\rho_i$  = impurity and  $\rho_m$  = magnetic contributions to the resistivity. For these two samples  $\rho_m$  is constant above  $T_N$  (only spin disorder scattering) which accounts for the observed curve. (ii) The resistivity as a function of temperature for both the blue and purple samples are plotted in the upper part of Fig. 16. The room temperature resistivity is higher (because the free electron concentration is lower) and the linear decrease in  $\rho$  with decreasing temperature reaches a minimum near 75°K, thereafter increasing to a constant value at low temperatures. The behavior below 75K is not, as yet, understood, but a critical scattering appears to play an important role.

The Hall effect was measured at room temperature for the purple sample (Gd<sub>.453</sub>Se<sub>.547</sub>) and the carrier concentration derived by assuming a simple band was  $n = (1.4 \pm .2) \times 10^{22} \text{ cm}^{-3}$ . It is possible to check the consistency of this number with other independent measurements as follows: If we assume that each Gd contributes one electron to the conduction band, simple valence arguments lead to the expression

$$N_o [3x - 2(1 - x)]^2 = n \quad (5.3.2)$$

where  $N_o$  = carrier concentration for the stoichiometric composition ( $x = 0.5$ ) and  $x$  = composition. Solving for  $N_o$ , using the experimental values  $x = 0.453$  and  $n = 1.4 \times 10^{22} \text{ cm}^{-3}$ , one obtains  $N_o = 2.6 \times 10^{22} \text{ cm}^{-3}$ . On the other hand we can also calculate  $N_o$  using the lattice parameter for stoichiometric material as  $N_o = 4/a_o^3 = 4/(5.79 \times 10^{-8})^3 = 2.1 \times 10^{22} \text{ cm}^{-3}$ . Better agreement

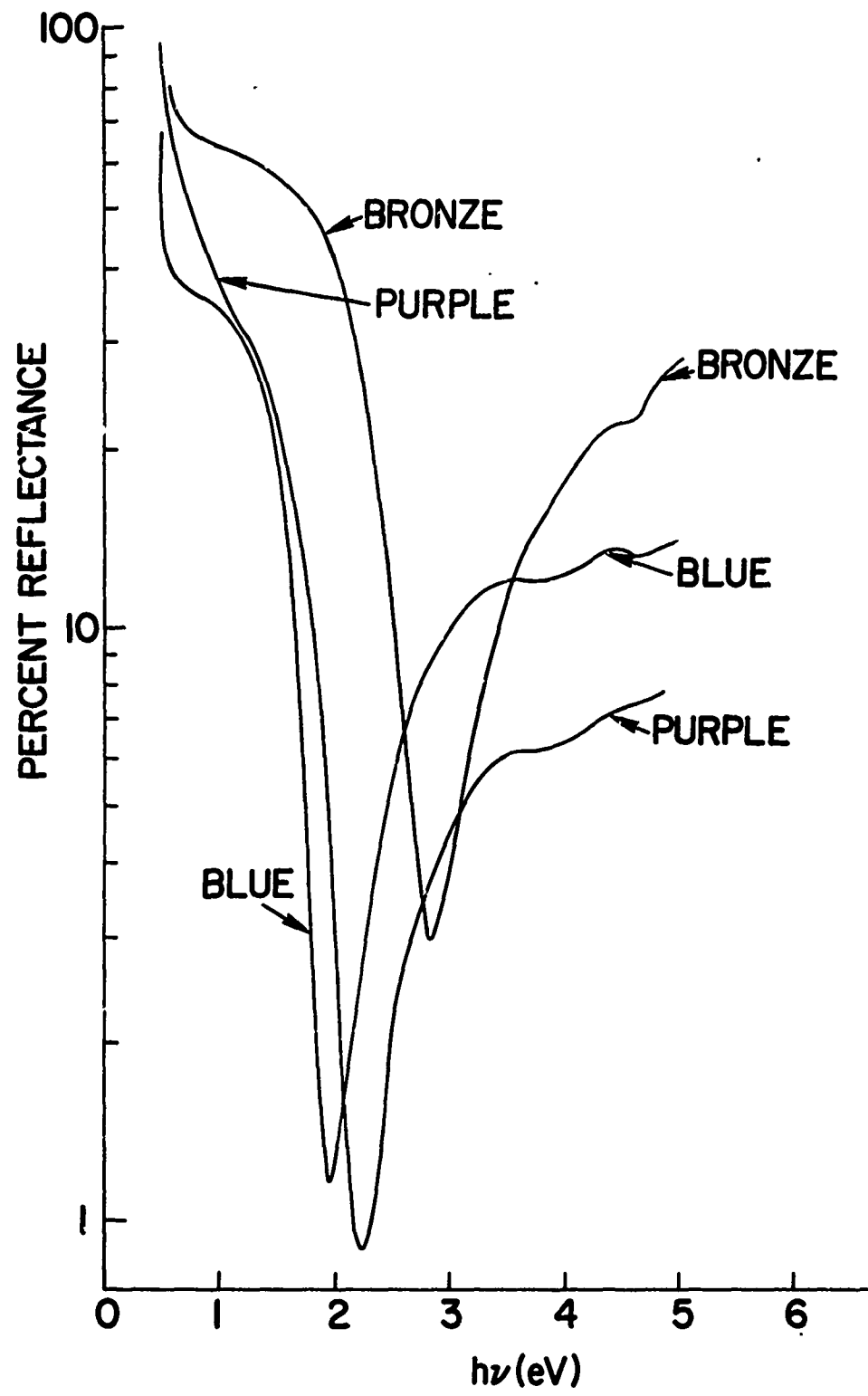


Figure 17. Percent reflectance  $R$  as a function of  $h\nu$ .

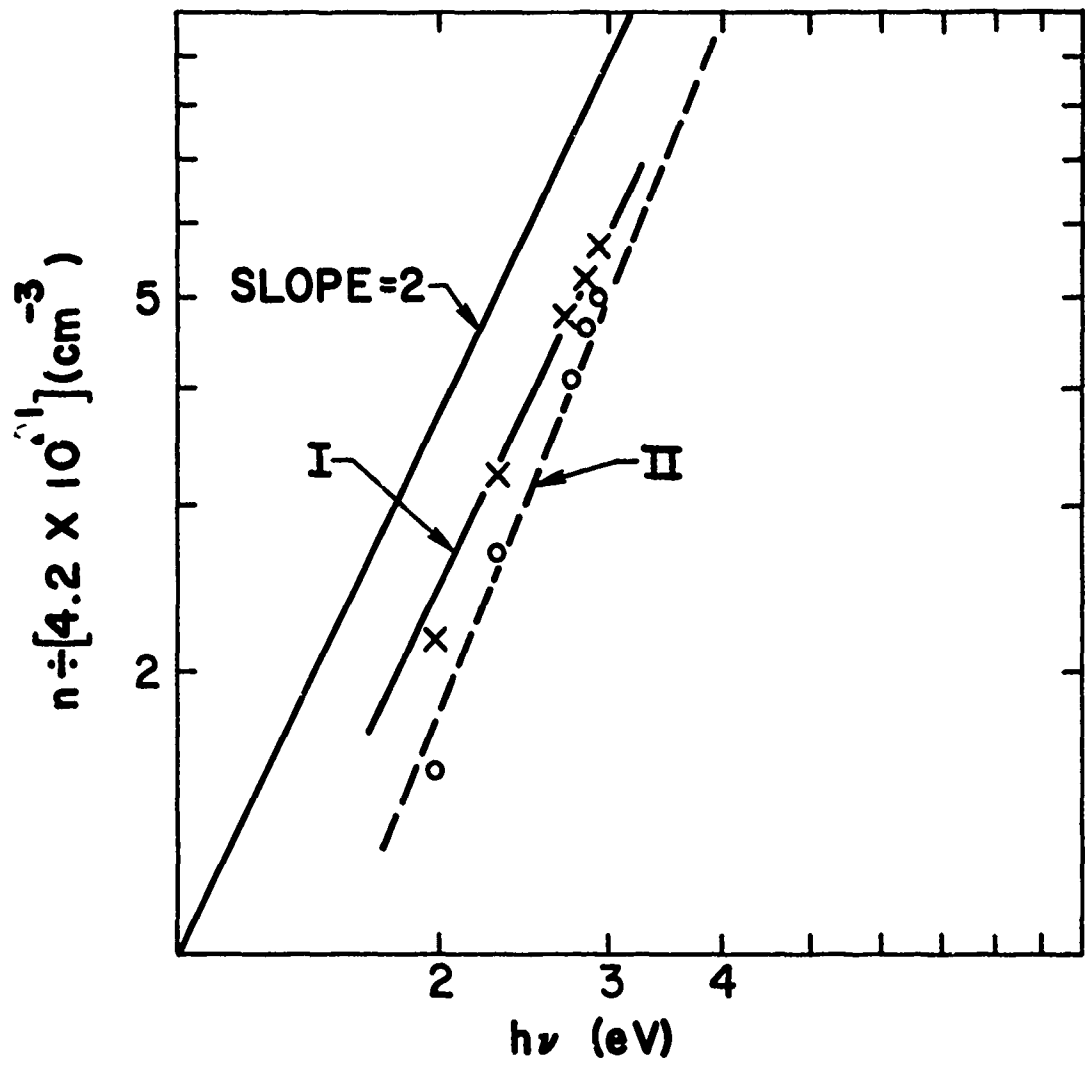


Figure 18. Carrier concentration,  $n$ , derived from experimental composition,  $x$ , (see text) as a function of  $h\nu$  for which the reflectivity is a minimum. The data is plotted on a log-log scale to demonstrate that  $n \propto (h\nu)^2$  in the  $\text{Gd}_x \text{Se}_{1-x}$  system.

can be obtained if we fix the absolute value of  $x$  by using wet chemical analysis. In this case  $x = 0.453$  is replaced by  $x = .465$  and  $N_0 = 2.2 \times 10^{22} \text{ cm}^{-3}$ . These results lends credence to our assumption that the number of free carriers is governed by stoichiometry.

It is also tempting to attribute the dramatic changes in color simply to changes in carrier concentration. Figure 17 shows reflectivity data for three representative samples. For the case that the reflectivity minimum,  $R_{\min}$ , is  $\leq 5\%$ , the dispersion relation for free carriers yields the following expression:

$$m_s \propto \frac{n \lambda_{\min}^2}{\epsilon_{\infty} - 1} \quad (5.3.3)$$

where  $m_s$  is the effective mass,  $\epsilon_{\infty}$  is normally the high frequency dielectric constant when considering semiconductors but is less well defined in the present case,  $n$  is the number of free carriers per unit volume and  $\lambda_{\min}$  is the wavelength at which  $R_{\min}$  occurs. Since  $v \propto \frac{1}{\lambda}$ , (4.3.3) can be rewritten as  $(hv)_{\min}^2 \propto n$ , and, assuming that  $m_s$  and  $\epsilon_{\infty}$  do not vary substantially throughout the series, a plot of  $\log n$  vs  $\log hv$  should yield a straight line with a slope equal to 2. We have assumed here that  $\lambda_{\min}$  is dominated by free carriers and that interband transitions, etc. contribute primarily to the shape of the reflectivity curve. Figure 18 exhibits the results of such a plot. Curves I and II differ only in the choice of absolute concentration,  $x$ , from which  $n$  is calculated.

All compositions in the solid solution system order antiferromagnetically. A rough measure of Néel temperatures indicates that they vary from  $\sim 20^\circ\text{K}$  for

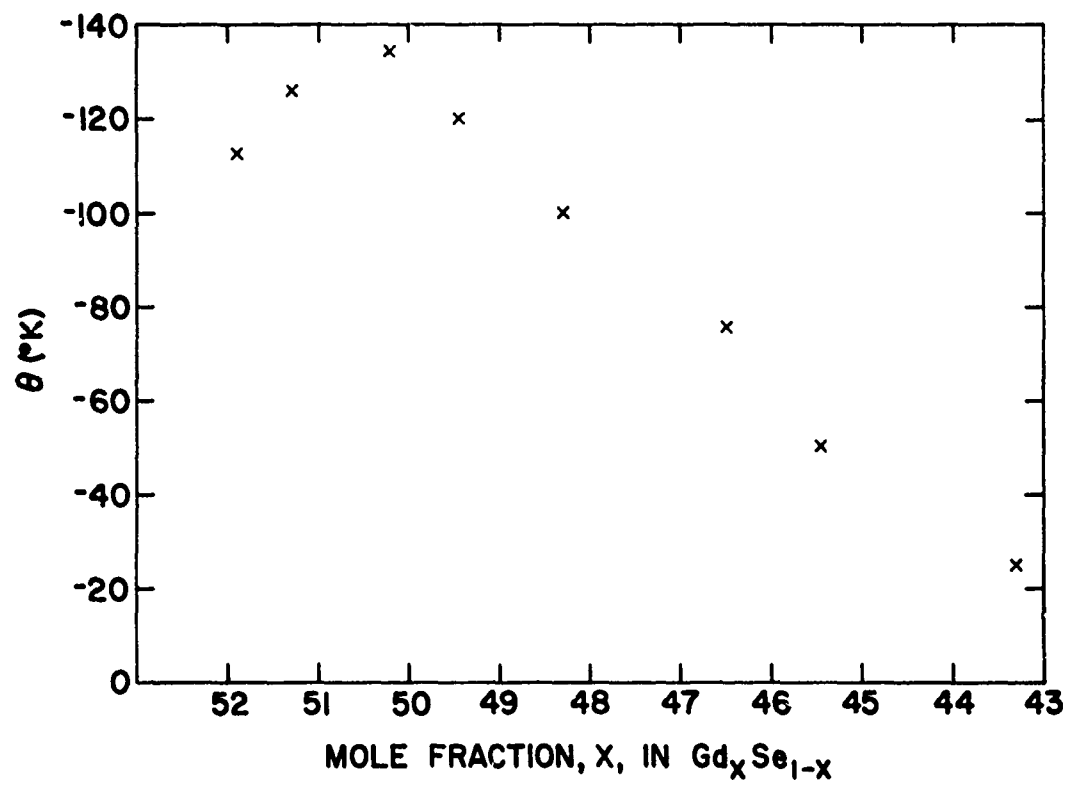


Figure 19. Paramagnetic Curie temperature,  $\theta$ , as a function of composition,  $x$ , for  $\text{Gd}_x\text{Se}_{1-x}$ .

$x = 0.434$  to  $\sim 60^{\circ}\text{K}$  for  $x = 0.500$ . A plot of paramagnetic  $\theta$  values as a function of composition (Fig. 19) has a maximum near the stoichiometric composition.

As we have shown, the relationship between observed experimental parameters and composition is surprisingly direct, and in the case of resistivity and reflectivity can be explained on the basis of carrier concentration changes brought about by variations in stoichiometry. The uncertainty in the absolute value of  $x$  is a critical factor in testing our model and we expect to resolve the question of composition by using improved sampling and analytical techniques.

## 6.0 MAGNETIC STUDIES OF RARE EARTH CHALCOGENIDE MIXED VALENCY SYSTEMS

### 6.1 Introduction

Our study of the magnetic properties of europium and gadolinium compounds is concerned with the effect of dilution of the magnetic ion and its relationship to the exchange interactions. The influence of electrical conductivity is also a part of this work. Specific compounds investigated are the  $\text{Eu}_{1-x}\text{La}_x\text{S}$  and  $\text{Yb}_{1-x}\text{Gd}_x\text{S}$  compositional systems. These systems are compared to  $\text{Eu}_{1-x}\text{Gd}_x\text{S}$  which was reported<sup>56</sup> previously.

Both  $\text{Eu}_{1-x}\text{La}_x\text{S}$  and  $\text{Yb}_{1-x}\text{Gd}_x\text{S}$  have the face centered cubic structure and form a continuous series of solid solutions, where  $x$  goes from zero to one. An important consideration is that these are mixed valency systems as found in  $\text{Eu}_{1-x}\text{Gd}_x\text{S}$ . The Eu and Yb are divalent while La and Gd are trivalent. Thus each system is electrically insulating for  $x = 0$  and becomes metallic over the range investigated here ( $.01 \leq x < 1$ ). The conduction electrons are donated by the trivalent ions and the number of such electrons are assumed proportional to  $x$ .

$\text{Eu}^{2+}$  and  $\text{Gd}^{3+}$  have a well localized spin only ( $S = 7/2$ ) magnetic moment in the 4f shell. The interactions between the magnetic ions give rise to both ferromagnetic and antiferromagnetic long range order in these systems. The strength of the interaction is attributed in part to electrons donated by Gd or La which give rise to an indirect exchange interaction between the  $\text{Eu}^{2+}$  ions. This mechanism must certainly be important for  $x < .01$ , since the ferromagnetic curie temperature ( $T_c$ ) is increased initially by a factor of three in both  $\text{Eu}_{1-x}\text{La}_x\text{S}$  and  $\text{Eu}_{1-x}\text{Gd}_x\text{S}$ . In general, however, we will not be concerned with the exact exchange mechanism but will attempt only to evaluate its sign and magnitude.

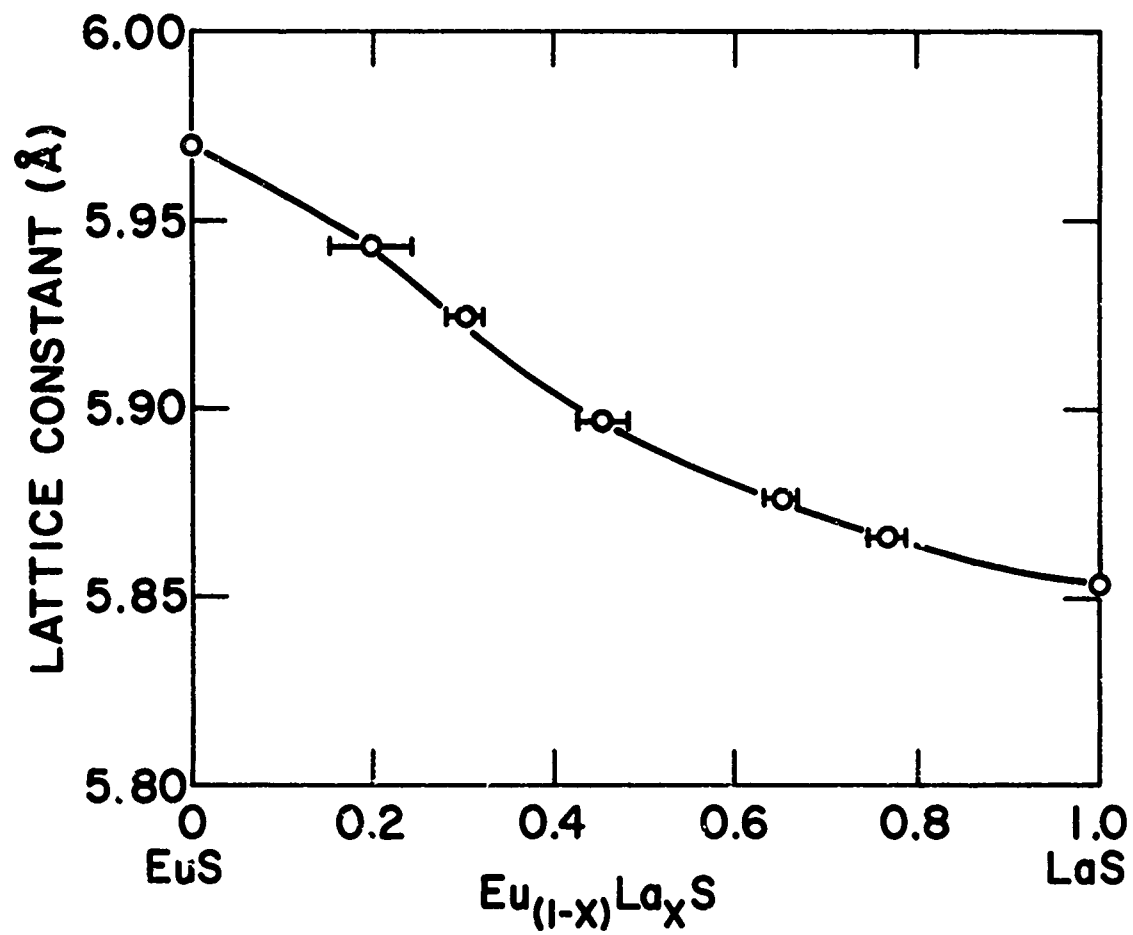


Figure 20. Lattice constant vs composition for  $\text{Eu}_{1-x}\text{La}_x\text{S}$ .

Information of this type can be obtained from the high temperature magnetic susceptibility ( $\chi$ ). Such data follow a Curie-Weiss law  $\chi = C/(T-\theta)$  where the Curie constant,  $C$ , is proportional to the square of the effective moment and  $\theta$  gives the sign of the magnitude of the exchange interactions. If we consider only a single interaction between nearest neighbor magnetic ions then  $\theta = 2/3 S(S+1) z J$ , where  $z$  is the number of nearest neighbors surrounding a given ion and  $J$  is the exchange energy.

In the original system studied ( $\text{Eu}_{1-x}\text{Gd}_x\text{S}$ ) three exchange interactions were introduced; Eu-Eu, Eu-Gd, and Gd-Gd. The two new compositional systems  $\text{Eu}_{1-x}\text{La}_x\text{S}$  and  $\text{Yb}_{1-x}\text{Gd}_x\text{S}$  simplify matters since each has only one interaction, i.e. either Eu-Eu or Gd-Gd. However, dilution effects also occur which must be taken into consideration.

## 6.2 Experimental

### 6.2.1 $\text{Eu}_{1-x}\text{La}_x\text{S}$ System

The starting material is EuS, whose ferromagnetic properties are well known ( $T_c = 16.5^\circ\text{K}$ ,  $\mu_B = 7$  Bohr magnetons per  $\text{Eu}^{2+}$ ). Lanthanum exists as an ion only in the trivalent form and is without moment. As far as is known,  $\text{La}^{3+}$  substitutes randomly for the  $\text{Eu}^{2+}$  and because of the similarity in ionic radii the lattice constant decreases only slightly, as indicated in Fig. 20.

Figures 21 and 22 show magnetic data for the  $\text{Eu}_{1-x}\text{La}_x\text{S}$  system. It is apparent that the magnetization curves measured at  $4.2^\circ\text{K}$  appear ferromagnetic for compositions only up to  $x = .5$ . For  $x \geq .65$  paramagnetism is dominant and measurements down to  $1.3^\circ\text{K}$  indicated no evidence of long range order in these compounds. This is further illustrated in Fig. 22 where both  $T_c$  and  $\theta$  are plotted as a function of composition. Note that the  $\theta$  value remains positive

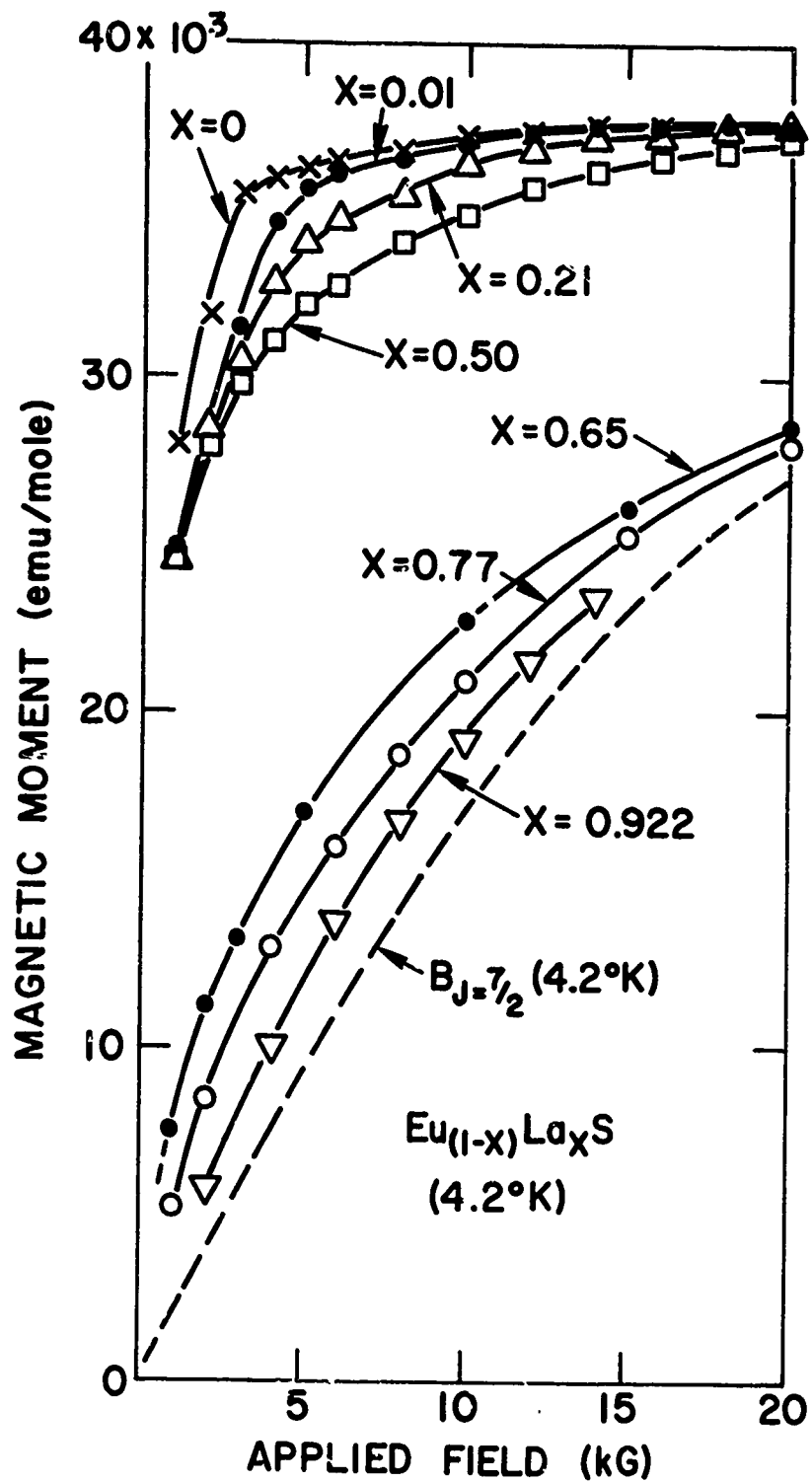


Figure 21. Magnetic moment vs applied magnetic field at  $4.2^\circ\text{K}$  for several compositions of  $\text{Eu}_{1-x}\text{La}_x\text{S}$ . The dotted curve marks  $B_J = 7/2$  is the Brillouin function calculated for pure paramagnetic behavior at  $4.2^\circ\text{K}$  as a comparison for compositions  $x \geq .65$ .

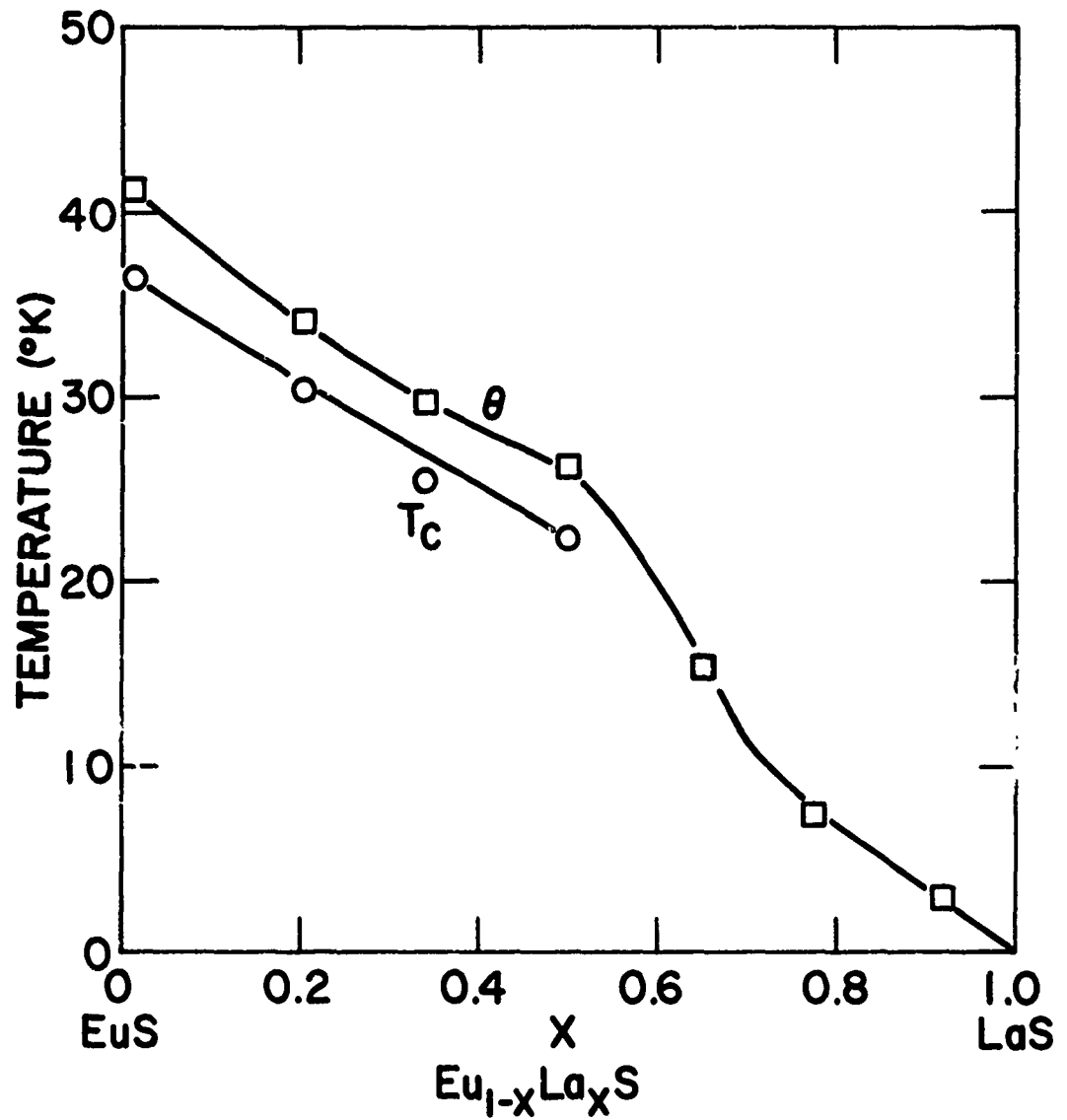


Figure 22. Curie temperature and paramagnetic  $\theta$  as a function of composition for  $\text{Eu}_{1-x}\text{La}_x\text{S}$ .

over the complete range of compositions, indicating that the Eu-Eu interaction remains ferromagnetic regardless of the dilution or increased electrical conductivity.

#### 6.2.2 $\text{Yb}_{1-x}\text{Gd}_x\text{S}$ System

Data on this system are not as complete as on the La-system, and more work is in progress. In this case  $\text{Gd}^{3+}$  contributes conduction electrons and magnetic moment, while  $\text{Yb}^{2+}$  is a non-magnetic replacement for  $\text{Eu}^{2+}$ . Table V shows the results so far obtained. It is clear from Table V that the exchange

$x$	$\theta$ ( $^{\circ}\text{K}$ )	$T_N$ ( $^{\circ}\text{K}$ )
0	-	-
.25	- 36	-
.50	- 42	< 20
.61	- 76	20
1.0	-125	50

Table V.  $\text{Yb}_{1-x}\text{Gd}_x\text{S}$

interactions must be negative since  $\theta$  is negative. Antiferromagnetic Néel temperatures are not listed for  $x \leq .5$  because of the difficulty of interpreting the susceptibility data which show no pronounced maximum or change in slope for these compositions.

#### 6.3 Discussion

In our earlier work on  $\text{Eu}_{1-x}\text{Gd}_x\text{S}$  we had arrived at a model which included positive Eu-Eu and Eu-Gd interactions and a negative Gd-Gd exchange. Our new data support this assignment and allow us to assign quantitative values for

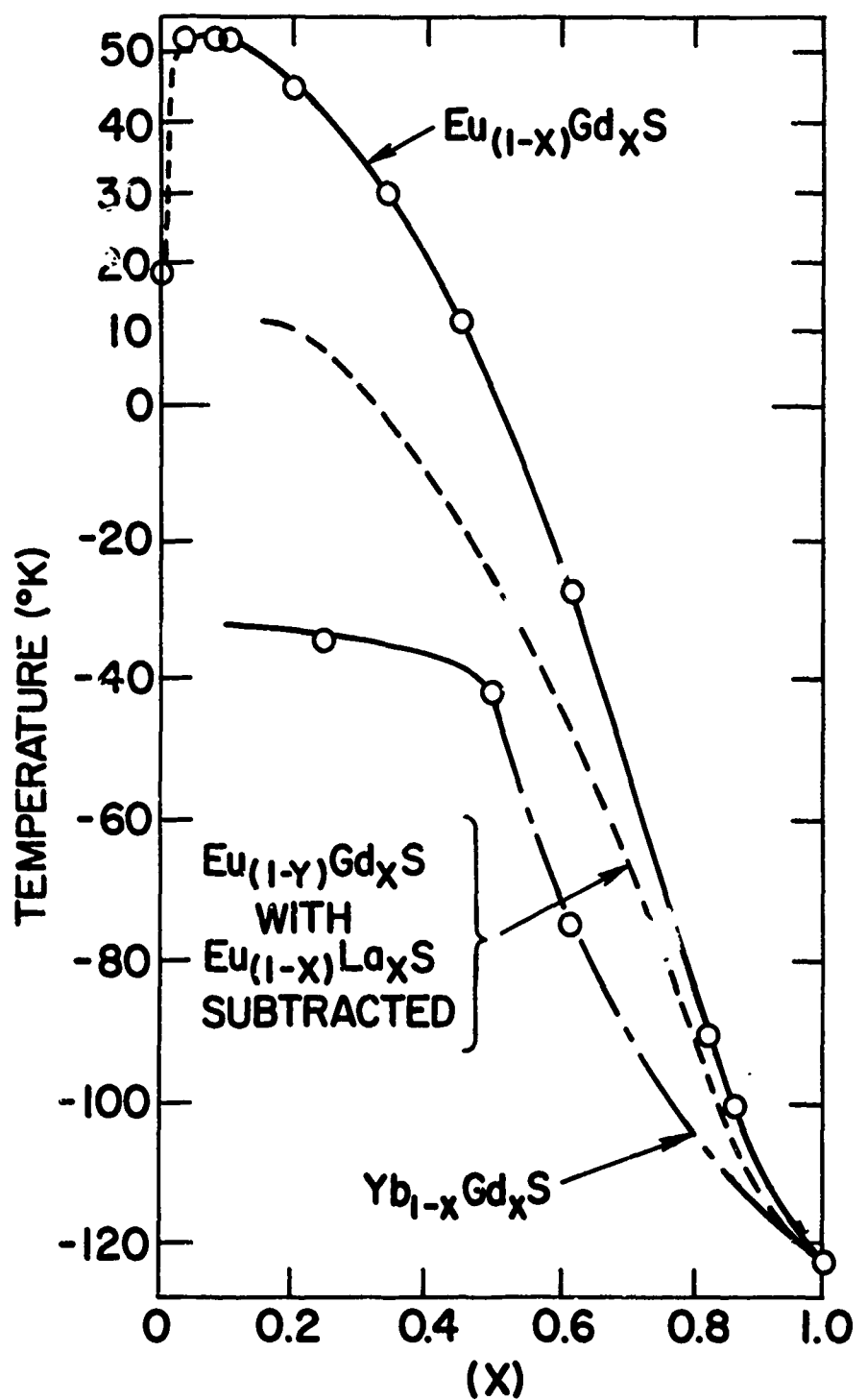


Figure 23. Paramagnetic  $\theta$  vs composition for  $\text{Eu}_{1-x}\text{Gd}_x\text{S}$  and  $\text{Yb}_{1-x}\text{Gd}_x\text{S}$ . The dashed curve is calculated as indicated above.

the exchange in each case. Such an assignment is shown in Table VI for the three systems, each at  $x = .5$ . The Eu-Gd exchange is calculated based on the

Exchange Interactions (°K)			
	Eu-Eu	Eu-Gd	Gd-Gd
$\text{Eu}_{.5}\text{Gd}_{.5}\text{S}$		+19	+3
$\text{Eu}_{.5}\text{La}_{.5}\text{S}$	+26		
$\text{Yb}_{.5}\text{Gd}_{.5}\text{S}$			-42

Table VI

algebraic sum of the other three values which are experimental and come from Table V and Figs. 22 and 23.

Figure 23 shows three curves which includes the  $\theta$  vs composition ( $x$ ) for the  $\text{Eu}_{1-x}\text{Gd}_x\text{S}$  system. The lower curve is a plot of the  $\text{Yb}_{1-x}\text{Gd}_x\text{S}$  system. The middle curve (dashed) represents the  $\text{Eu}_{1-x}\text{Gd}_x\text{S}$  data after the  $\text{Eu}_{1-x}\text{La}_x\text{S}$  data have been subtracted off. The positive displacement of the dashed curve, which contains both Eu-Gd and Gd-Gd interactions, from the lower curve which contains only Gd-Gd interactions indicates that the Eu-Gd interactions is evidently positive for all compositions studied. Figure 23 puts in graphical form data found in Table VI, where only a single composition was discussed.

The interpretation of exchange interactions in these mixed valency systems in terms of three independent exchange interactions which depend only on the ion type has an important bearing on the nature of the exchange in these compounds. It has always been assumed that, because conduction electrons were present, interactions via the electrons should be long range. Thus  $\text{Eu}^{2+}$  and  $\text{Gd}^{3+}$  having the same spin-only moment might be expected to have some similarities

under similar conduction electron densities per magnetic ion (e.g. at  $x = .5$ ). However, this appears not to be the case and short range exchange interactions assume a greater importance than has previously been recognized.

Similar arguments concerning the short range nature of the exchange interactions in these metallic compounds can also be used in considering the effects of dilution. Certainly in  $Eu_{1-x}La_xS$  and perhaps also in  $Yb_{1-x}Gd_xS$  the composition  $x = .5$  marks the limit of long range order. In the La case theoretical analysis by de Gennes et al<sup>57</sup> indicates that long range order should extend to concentrations of  $x \approx .85$ . However, the analysis depends on the range of coupling and the short range interaction discussed previously may be an important consideration.

The monotonic decrease in  $\theta$  from  $42^\circ K$  to 0 in the La system and from  $-125^\circ K$  to 0 in the Yb system is merely indication<sup>58</sup> of the statistical change in the number of nearest neighbors  $z$  as a function of  $x$ . Thus  $\theta(x) = 2/3S(S+1)(1-x)z J(x)$ , where we indicate that the exchange energy can change with  $x$  because the lattice constant changes and the distance between magnetic ions will vary. In the La system, however, the lattice constant varies only slightly with composition (Fig. 20) and effects on the exchange parameter  $J$  can probably be neglected.

## REFERENCES

1. B. T. Matthias, R. M. Bozorth, and J. H. Van Vleck, Phys. Rev. Letters 7, 160 (1961).
2. N. Menyuk, K. Dwight, and T. B. Reed, Phys. Rev. B3, 1689 (1971).
3. J. C. Suits, Proc. Int. Conf. on Ferrites, Kyoto, Japan, 1970.
4. J. O. Dimmock, IBM J. Res. Develop. 14, 301 (1970).
5. G. Guntherodt, P. Wachter, and D. M. Imboden, Phys. Kondens. Materie. 12, 292 (1971)
6. M. R. Oliver, Thesis, Dept. of Electrical Engineering, M.I.T., June 1970, unpublished; and M. R. Oliver, J. D. Dimmock, A. L. McWhorter, and T. B. Reed, Phys. Rev. B, (1972).
7. T. Penney, M. W. Shafer, and J. B. Torrance, to be published, ibid., B, (1972).
8. G. Petrich, S. von Molnar, and T. Penney, Phys. Rev. Letters 26, 885 (1971).
9. M. W. Shafer and T. R. McGuire, J. Appl. Phys. 39, 588 (1968).
10. K. Y. Ahn and M. W. Shafer, ibid., 41, 1260 (1970).
11. C. F. Guerci and M. W. Shafer, ibid., 37, 1406 (1966).
12. T. B. Reed and R. E. Fahey, J. Crystal Growth 8, 337 (1971).
13. R. Verreault, Solid State Comm. 7, 1653 (1969).
14. G. Busch, R. Verreault, and O. Vogt, ibid., 8, 617 (1970).
15. C. Paparoditis, R. Suryanarayanan, C. Llinares, E. Monteit, and G. Boudre, ibid., 9, 1871 (1971).
16. M. W. Shafer, J. B. Torrance, and T. Penney, Proc. 17<sup>th</sup> Conf. on Magnetism and Magnetic Materials, Chicago, 1971.
17. M. W. Shafer, J. Appl. Phys. 36, 1145 (1965).
18. J. M. Haschke and H. A. Eick, J. Phys. Chem. 73, 374 (1969).
19. 3<sup>rd</sup> Quarterly Report, Contract AF19(628)-5167, Lincoln Lab., Solid State Division, p. 15-21 (1969).

20. R. G. Bedford and E. Catalano, *J. Solid State Chem.* 3, 112 (1971).
21. G. McCarthey and W. B. White, *J. the Less-Common Metals* 22, 409 (1970).
22. G. Petrich, private communication.
23. M. W. Shafer and C. F. Guerci, *Abstract, 67<sup>th</sup> Annual Meeting, J. Amer. Ceram. Soc., Philadelphia, 1965.*
24. A. Muan, *Am. J. Science* 256, 171 (1958).
25. S. von Molnar and T. Kasuya, *Proc. 10<sup>th</sup> Int. Conf. on Phys. Semiconductors*, S. P. Keller, J. C. Hensel, and F. Stern, eds., Conf. 700 801 (U.S. AEC Div. of Tech. Info., Oak Ridge, Tenn., 1970), p. 233.
26. G. H. Dieke, *Spectra and Energy Levels of Rare Earth Ions in Crystals* (Interscience, New York, 1968).
27. J. B. Torrance and M. W. Shafer, to be published.
28. S. von Molnar, *IBM J. Res. Develop.* 14, 269 (1970).
29. This procedure is justifiable since the ratio of the four- to two-probe values is the same at both high and low temperatures for sample IV-5.
30. S. von Molnar and M. W. Shafer, *J. Appl. Phys.* 41, 1093 (1970).
31. Private communication.
32. N. F. Mott, *J. Non-Cryst. Solids* 1, 1 (1968).
33. T. Kasuya, *IBM J. Res. Develop.* 14, 214 (1970); T. Kasuya and A. Yanase, *Rev. Mod. Phys.* 40, 1684 (1968).
34. R. Tsu and L. Esaki, *Phys. Rev. Letters* 24, 455 (1970).
35. E. Kaldis, J. Schoenes, and P. Wachter, to be published.
36. N. F. Mott and E. A. Davis, "Electronic Processes in Non-Crystalline Materials," Clarendon Press, Oxford (1971).
37. S. von Molnar and T. Kasuya, *Phys. Rev. Letters*, 21, 1757 (1968).

38. S. von Molnar and T. Kasuya, Proc. 10th Intl. Conf. Phys. Semiconductors, 233 (1970; Y. S. Shapira and T. B. Reed, Phys. Rev., B5, 4877 (1972).
39. E. O. Kane, Phys. Rev., 131, 79 (1963).
40. T. P. Eggarter and M. H. Cohen, Phys. Rev. Letters, 25, 807 (1970); R. Zallen and H. Scher, Phys. Rev., B4, 4471 (1971); S. Kirkpatrick, Phys. Rev. Letters, 27, 1722 (1971).
41. D. Redfield, Phys. Rev. Letters, 27, 730 (1971).
42. M. Cutler and N. F. Mott, Phys. Rev., 181, 1336 (1969).
43. V. Ambegaokar, B. I. Halperin and J. S. Langer, Phys. Rev., B4, 2612 (1971).
44. V. K. S. Shante, unpublished.
45. W. A. Thompson et al, 11th Intl. Conf. Phys. Semiconductors, Warsaw (1972).
46. T. Holstein and L. Friedman, Phys. Rev., 165, 1019 (1968); D. Emin and T. Holstein, Ann. Phys. (New York), 53, 439 (1969); D. Emin, Ann. Phys. (New York), 64, 336 (1971); D. Emin, C. H. Seager and R. K. Quinn, Phys. Rev. Letters, 28, 813 (1972).
47. L. Friedman, J. Non-Cryst. Sol., 6, 329 (1971).
48. Landolt-Börnstein Tables, K.-H. Hellwege and A. M. Hellwege eds., 4a, pp. 41-109, Springer, New York (1970).
49. M. Cutler, J. F. Leavy and R. I. Fitzpatrick, Phys. Rev., 133, A1143 (1964); M. Cutler and J. F. Leavy, Phys. Rev. 133, A1153 (1964); M. Cutler and N. F. Mott, Phys. Rev., 181, 1336 (1969).
50. P. G. de Gennes, Phys. Rev., 118, 141 (1960).
51. E. H. Putley, "The Hall Effect and Related Phenomena," Butterworth, London (1960).
52. Olov Lindberg, Proc. I.R.E., 40, 1414 (1952).

53. S. von Molnar and T. Kasuya, Proc. 10th Intl. Conf. on Phys. of Semiconductors, S. P. Keller, J. C. Hensel, F. Stern, eds., Conf. 700, 801, U. S. AED Div. of Tech. Inf., Oak Ridge, Tenn., (1970, p. 233).
54. J. M. Lavine, Phys. Rev., 123, 1273 (1961).
55. M. Guittard and J. Flahaut, Bull. Soc. Chim., p. 4759 (1968).
56. T. R. McGuire and F. Holtzberg, AIP Conf. Proc., #5, p. 855 (1971).
57. P. G. de Gennes, P. Lafore and J. P. Millot, J. Phys. Chem. Solids, 11, 105 (1959).
58. J. S. Smart, J. Phys. Chem. Solids, 16, 169 (1960).

**END**